A RATIONAL BASIS FOR CIRCUMFERENTIAL DISTORTION INDEX FORMULATION

Charles Patrick Downs

NAVAL POSTGRADUATE SCHOOL
Monterey, California

THESIS

A RATIONAL BASIS FOR CIRCUMFERENTIAL DISTORTION INDEX FORMULATION

by

Charles Patrick Downs

June 1974

Thesis Advisor: A. E. Fuhs

UNCLASSIFIED

SECURITY CLASSIFICATION OF THIS PAGE *(When Data Entered)*

REPORT DOCUMENTATION PAGE		READ INSTRUCTIONS BEFORE COMPLETING FORM
1. REPORT NUMBER	2. GOVT ACCESSION NO.	3. RECIPIENT'S CATALOG NUMBER
4. TITLE *(and Subtitle)* A Rational Basis for Circumferential Distortion Index Formulation		5. TYPE OF REPORT & PERIOD COVERED Master's Thesis June 1974 6. PERFORMING ORG. REPORT NUMBER
7. AUTHOR*(s)* Charles Patrick Downs		8. CONTRACT OR GRANT NUMBER*(s)*
9. PERFORMING ORGANIZATION NAME AND ADDRESS Naval Postgraduate School Monterey, California 93940		10. PROGRAM ELEMENT, PROJECT, TASK AREA & WORK UNIT NUMBERS
11. CONTROLLING OFFICE NAME AND ADDRESS Naval Postgraduate School Monterey, California 93940		12. REPORT DATE June 1974 13. NUMBER OF PAGES 76
14. MONITORING AGENCY NAME & ADDRESS*(if different from Controlling Office)* Naval Postgraduate School Monterey, California 93940		15. SECURITY CLASS. *(of this report)* UNCLASSIFIED 15a. DECLASSIFICATION/DOWNGRADING SCHEDULE

16. DISTRIBUTION STATEMENT *(of this Report)*

Approved for public release; distribution unlimited.

17. DISTRIBUTION STATEMENT *(of the abstract entered in Block 20, if different from Report)*

18. SUPPLEMENTARY NOTES

19. KEY WORDS *(Continue on reverse side if necessary and identify by block number)*

Compressor Stall
Compressor Surge
Compressor Instability
Distortion Index
Vorticity

20. ABSTRACT *(Continue on reverse side if necessary and identify by block number)*

NASA has recently published data on the effects of temperature and pressure distortion on the stability of axial-flow compressors. Theoretical predictions of compressor instability based on vorticity do not explain the observed compressor stability of the NASA tests. Description of distorted flow by vorticity is extended by a simplified model which incorporates vortex sheets and influence coefficients.

DD FORM 1 JAN 73 1473 EDITION OF 1 NOV 65 IS OBSOLETE
S/N 0102-014-6601 | 1
(Page 1)

UNCLASSIFIED
SECURITY CLASSIFICATION OF THIS PAGE *(When Data Entered)*

Block #20 continued

To determine the upstream influence of the compressor on flow field distortion, a model using parallel compressor theory, experimental data from NASA and a pressure ratio equation derived by Hill and Peterson is formulated. The model correctly predicts compressor blade loading calculated by Carta. This new model accounts for upstream effects of the compressor and shows that the vorticity model by itself is incomplete. Incorporation of the new model into a distortion index based on radial vorticity and total pressure change is proposed and discussed.

A Rational Basis for Circumferential Distortion Index Formulation

by

Charles Patrick Downs
Lieutenant Commander, United States Navy
B.S. ASE, University of Oklahoma, 1961

Submitted in partial fulfillment of the
requirements for the degree of

MASTER OF SCIENCE IN AERONAUTICAL ENGINEERING

from the

NAVAL POSTGRADUATE SCHOOL
June 1974

ABSTRACT

NASA has recently published data on the effects of temperature and pressure distortion on the stability of axial-flow compressors. Theoretical predictions of compressor instability based on vorticity do not explain the observed compressor stability of the NASA tests. Description of distorted flow by vorticity is extended by a simplified model which incorporates vortex sheets and influence coefficients. To determine the upstream influence of the compressor on flow field distortion, a model using parallel compressor theory, experimental data from NASA and a pressure ratio equation derived by Hill and Peterson is formulated. The model correctly predicts compressor blade loading calculated by Carta. This new model accounts for upstream effects of the compressor and shows that the vorticity model by itself is incomplete. Incorporation of the new model into a distortion index based on radial vorticity and total pressure change is proposed and discussed.

TABLE OF CONTENTS

LIST OF FIGURES

LIST OF SYMBOLS

a - speed of sound

c_p - specific heat at constant pressure

D - diameter

M - Mach number

$\dot{m}$ - mass flow rate

N - rotational speed, revolutions per minute

r - radius

R - gas constant

R_e - Reynolds number

P - pressure (static)

P_t - total pressure (stagnation temperature)

T_t - total temperature (stagnation temperature)

T - temperature (static)

U - absolute velocity

W - velocity relative to compressor blade row

$\dot{W}$ - weight flow

α - blade angle of attack

β - inlet flow angle

γ - ratio of specific heats

δ - ratio of actual pressure to NASA reference pressure

θ - ratio of actual temperature to NASA reference temperature

θ^* - circumferential position coordinate

λ - cascade stagger angle

Π_c - compressor total pressure ratio

ρ - density

σ - stall angle parameter

ω - fluid vorticity

Ω - rotational speed (radians/time)

SUBSCRIPTS

r - radial direction on compressor face

θ^* - circumferential direction on compressor face

z - axial direction, longitudinal axis of compressor or turbo-jet engine.

ACKNOWLEDGEMENT

During his course of instruction at the Naval Postgraduate School, the author suffered an accident that required hospitalization and convalescence. The flexible response by the entire faculty of the Department of Aeronautics in formulating an academic program that allowed the author to continue his studies is sincerely appreciated. The patience shown by Professor Allen E. Fuhs and his willingness to contribute a large amount of time, his most precious commodity, were invaluable during this research.

I. INTRODUCTION

In applications of high-specific-energy turbomachines, such as turbo-jet engines with axial-flow compressors, it is necessary to operate the compressor as close to maximum pressure ratio as possible without inducing unstable performance known as surge. A phenomenon of axial flow compressors is sensitivity to non-uniform or distorted flow fields when operating near maximum pressure ratio. As aircraft are designed for higher speeds and more comprehensive operating envelopes, the possibility of flow field distortion at the compressor face is increased. At supersonic speeds, shock effects within the engine intake system are significant. At high altitudes and low Mach numbers the effects of low Reynolds number may cause portions of the flow in the compressor to revert to laminar flow. Laminar flow increases the tendency toward separation which accelerates compressor stall. Aircraft operations at high angles of attack and/or yaw also can cause distortions of the flow field. High performance military aircraft may be subjected to all of the above distortions in addition to armament related temperature distortions. Forward firing armament could also cause ingestion of foreign gas into the compressor and is discussed in Appendix A. Compressor surge is not restricted to the airborne flight envelope. Ground operations with some recently developed engines have resulted in

destructive surge while taxiing. Figure 1 shows some of the general areas of the flight envelope where large stability margins are required. Figure 2 shows a compressor map that illustrates the stability margin. The associated performance penalty of a large stability margin becomes more acute as engine performance requirements increase.

This situation has motivated the formulation of a distortion index that could be used in the design, development, and component matching of turbo-jet engines which use axial-flow compressors. Conceivably such an index could be used in engine control systems to allow operation at reduced stability margins without the danger of compressor stall.

Several approaches to distortion indices have been tried. In fact there has been a proliferation of indices based on pressure distortion or temperature distortion at the face of the compressor. Most data collected are in the form of total pressure or total temperature measured at the compressor face. A more recent approach is to formulate an index based on vorticity. Since vorticity can be derived from either temperature or pressure data, a single index appropriate for both forms of distortion is possible.

Farmer [Ref. 1] investigated converting total-pressure fluctuations at the compressor face into vorticity. Iverson [Ref. 2] proposed a method of transforming total-temperature contours into vorticity. Shoemaker [Ref. 3] expanded Farmer's theory and, using a computer generated map of vorticity, derived an index, based on vorticity alone, that predicted

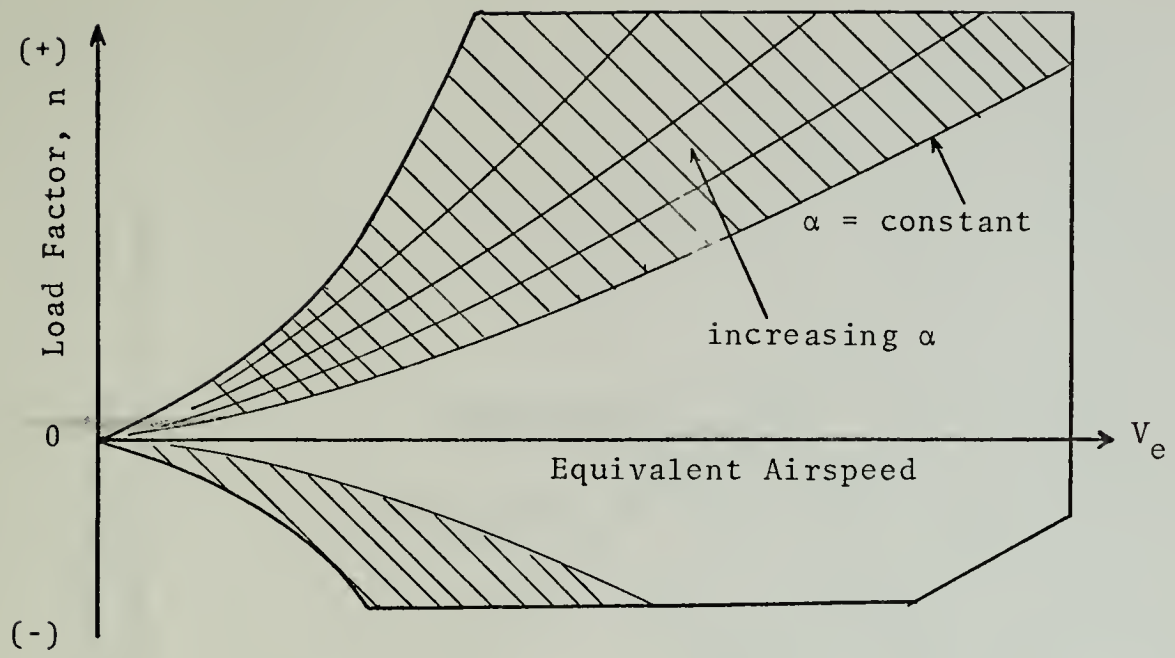

(a) Maneuvering Flight.

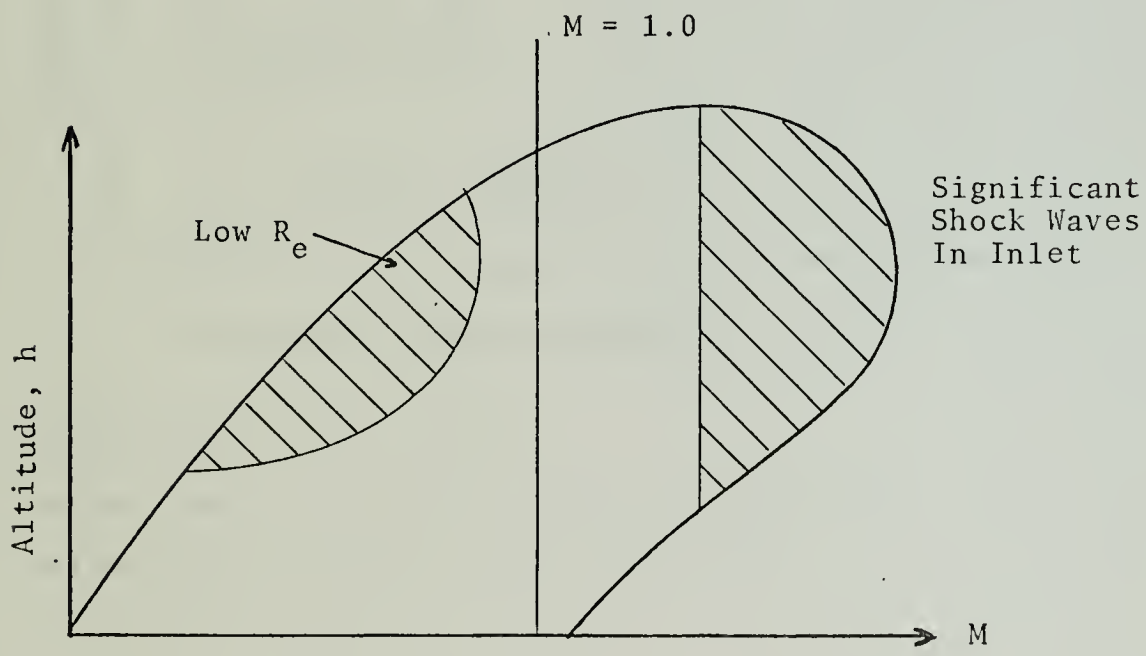

(b) Cruise Flight.

Figure 1. Flight Envelopes Showing Areas of Potential Compressor Instability.

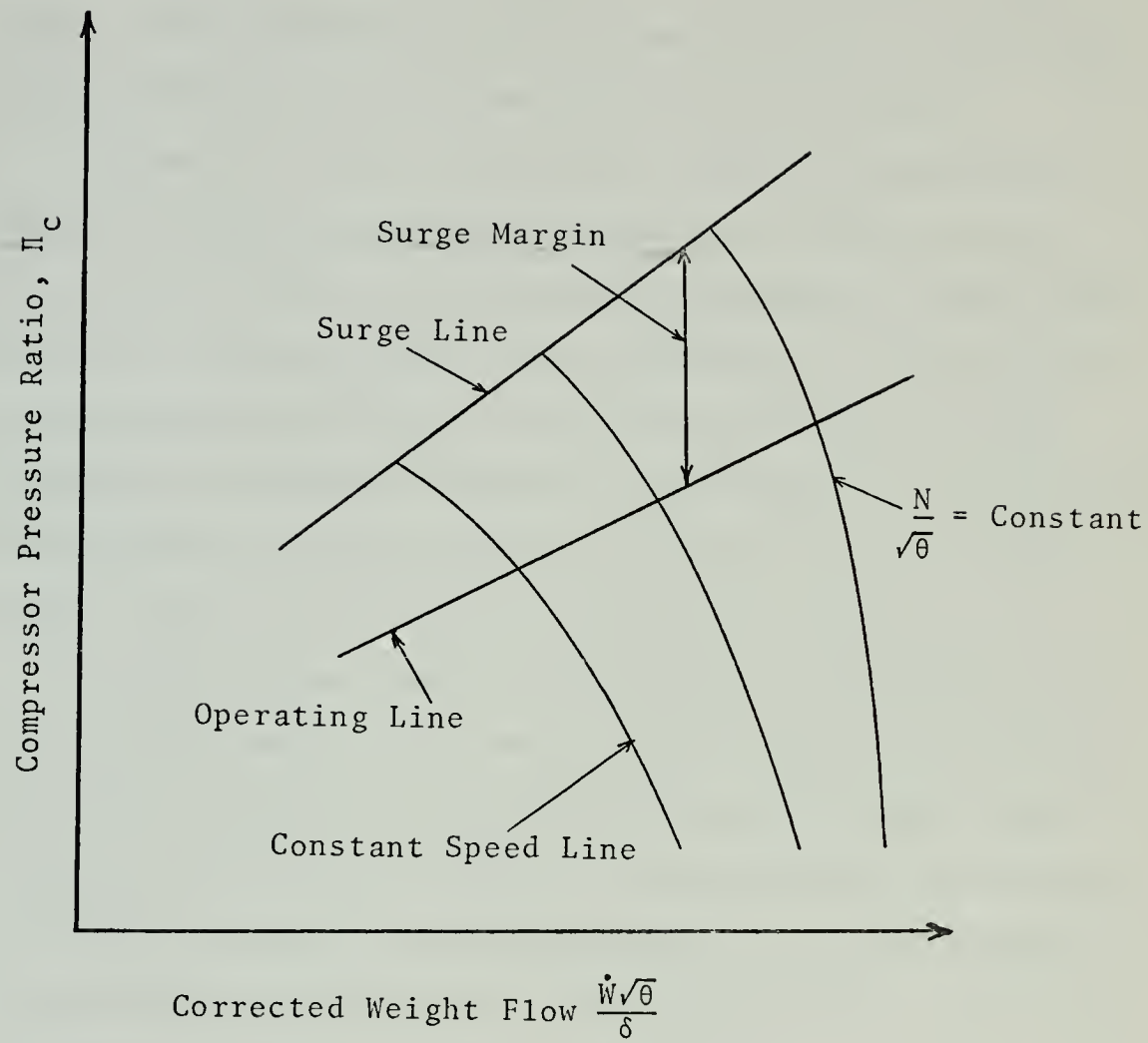

N = compressor rotation speed

θ = actual temperature/NASA reference temperature

δ = actual pressure/NASA reference pressure

Figure 2. Typical Axial-Flow Compressor Performance Map.

stall in selected stall events. Research conducted, concurrent with this paper, by Vann [Ref. 4], refines the Shoemaker vorticity index and applies it to additional stall events. The refined vorticity index (Vann) is an accurate stall predictor in 45 percent of the cases studied.

Braithwaite, Graber and Mehalic [Ref. 5] address the effects of inlet temperature and pressure distortion on turbo-jet performance and provide experimental results with which the vorticity model can be compared. In the case of total-pressure distortion, the vorticity model is a good predictor of decreased compressor performance. The vorticity model based on total-temperature distortion does not correlate well in all cases when compared with Ref. 5.

To gain further insight into this apparent failure of the vorticity model to correlate with experimental results, this paper will apply the vorticity model to models simulating the conditions of Ref. 5. In addition, an extended model that includes the engine effects on the upstream flow field will be introduced and a new approach to a distortion index will be discussed.

II. THE NATURE OF THE PROBLEM

The vorticity approach of Farmer, Iverson and Fuhs [Ref. 6] gives the following relationships for pressure and temperature distortion:

$$\omega'_r = \frac{1}{U'_z \gamma P' r'} \frac{\partial P'}{\partial \theta^*} \tag{1}$$

$$\omega'_r = \frac{M}{2r'} \frac{\partial T'}{\partial \theta^*} \tag{2}$$

where variables with superscripts (primed) are non-dimensionalized quantities as defined below:

$r = r' \frac{D}{2}$ D = compressor diameter

$U = U' \bar{a}$ $\bar{a}$ = average speed of sound

$\omega = \omega' \frac{2\bar{a}}{D}$ ω = fluid vorticity

$P_t = P' \bar{P}_t$ $\bar{P}_t$ = average stagnation pressure

$T_t = T' \bar{T}_t$ $\bar{T}_t$ = average stagnation temperature.

The subscripts θ^* and r denote circumferential and radial directions, respectively. A complete list of symbols is included on pages 8 and 9.

From the relationships given in Ref. 6, it also can be shown that in the case of combined pressure and temperature distortions

$$U_z \omega_r - U_r \omega_z = \frac{RT}{r P_t} \frac{\partial P_t}{\partial \theta^*} + \left[\frac{\frac{\gamma-1}{2} M^2}{1 + \frac{\gamma-1}{2} M^2} \right] c_p \frac{1}{r} \frac{\partial T_t}{\partial \theta^*} \quad . \tag{3}$$

Order of magnitude analysis [Ref. 6] indicates that $U_r\omega_z$ is of negligible size. Reference 5 compares the effects of pressure and temperature distortion, separately and in combination, on the performance of J85-GE-13 turbo-jet engines. To induce total-pressure distortions on the face of the compressor, screens of varying solidity and 180° circumferential extent (semi-circle) were placed one diameter upstream from the compressor. The total temperature of the air was distorted by means of a hydrogen burner, also of 180° extent, located four diameters upstream from the engine inlet. The burners were external to the bellmouth. The test procedure is discussed in detail in Ref. 5. Figure 3 shows a simplified schematic of the test set-up used. Figure 4 is a compressor map showing the degradation of performance associated with three combinations of pressure and temperature distortion at the engine inlet. From Fig. 4 the most adverse effect on compressor performance is observed to be the case of temperature and pressure distortions super-imposed (180° overlapped). Figure 5 shows the circumferential profiles of total temperature and total pressure at the engine inlet.

Based on the vorticity approach to distorted flow, one would expect that large values of ω_r would correlate with large loss of stall margin. Radial vorticity can be calculated from Eqn. (3). When $\partial P_t/\partial\theta^*$ and $\partial T_t/\partial\theta^*$ have the same algebraic sign, one would expect the most unfavorable case. Reference to Fig. 5(a) shows that for the 180° overlapped case, $\partial P_t/\partial\theta^*$ and $\partial T_t/\partial\theta^*$ have opposite signs; for this case

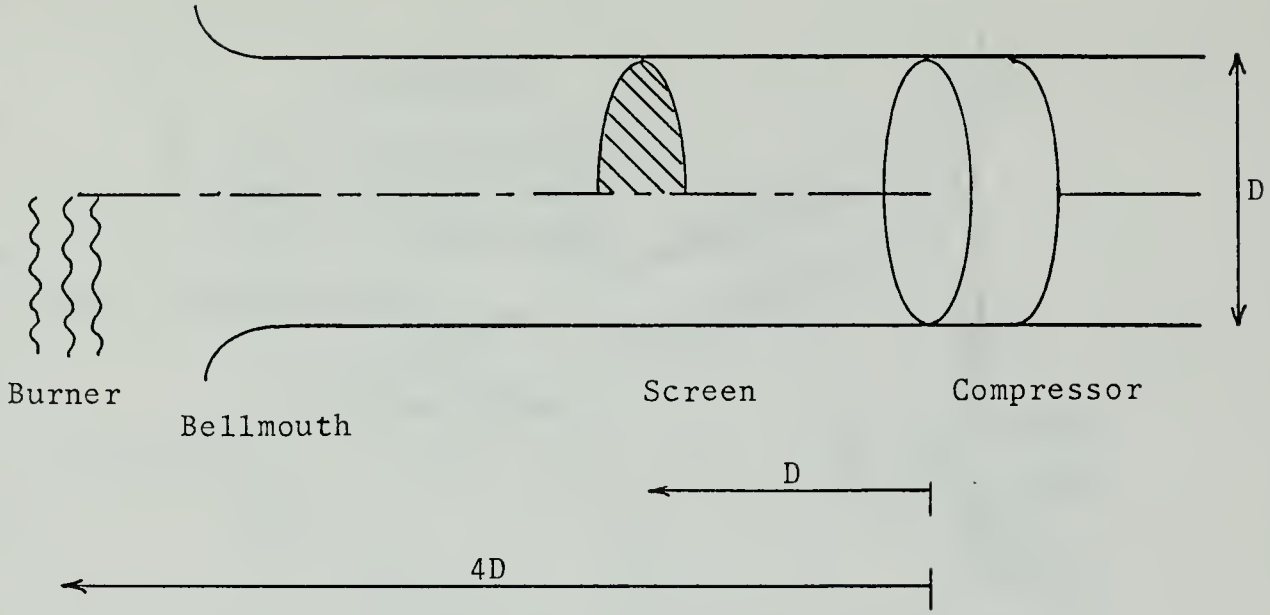

Figure 3. Schematic of Test Set-Up Used to Impose Distortion Flow Field At Compressor Inlet.

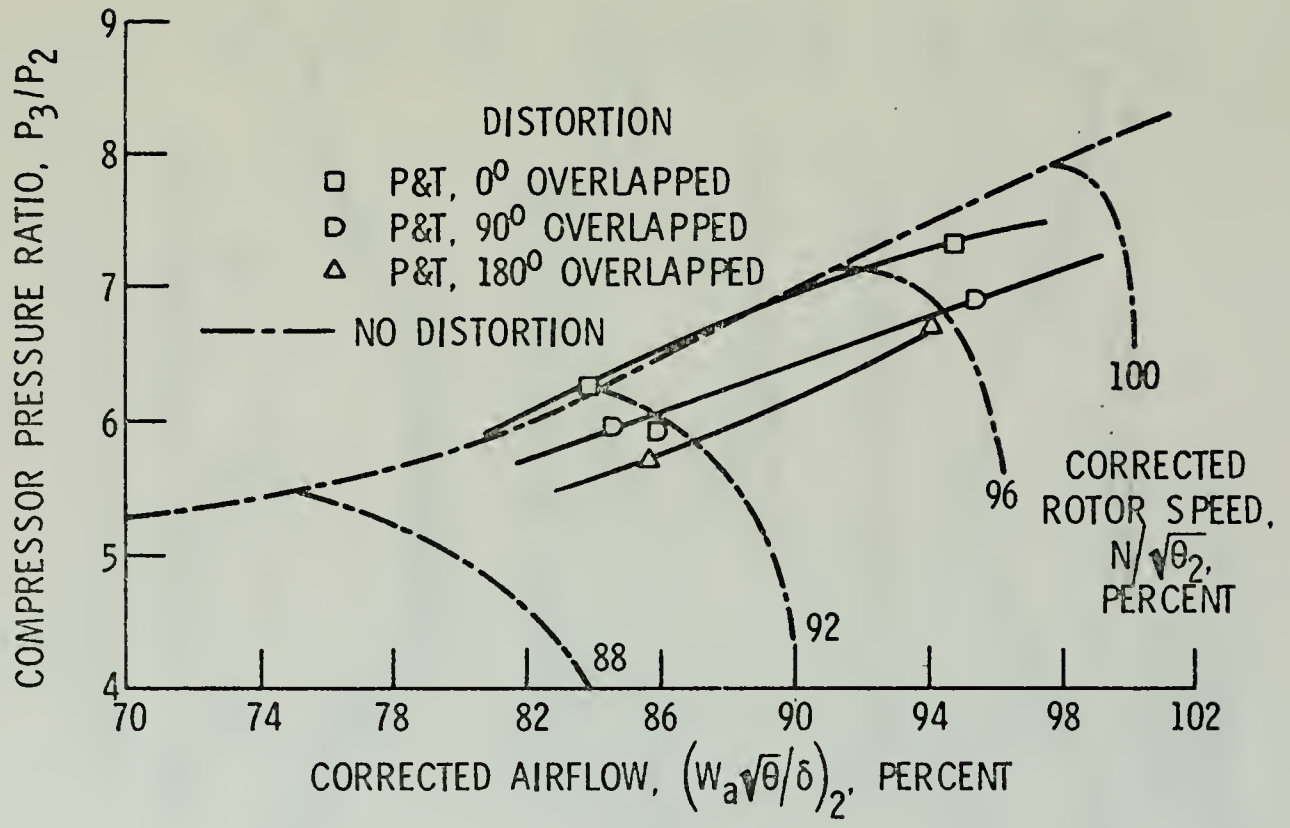

Figure 4. Compressor Map Showing Effects of 180° Extent Combined Pressure and Temperature Distortion (From Ref. 5).

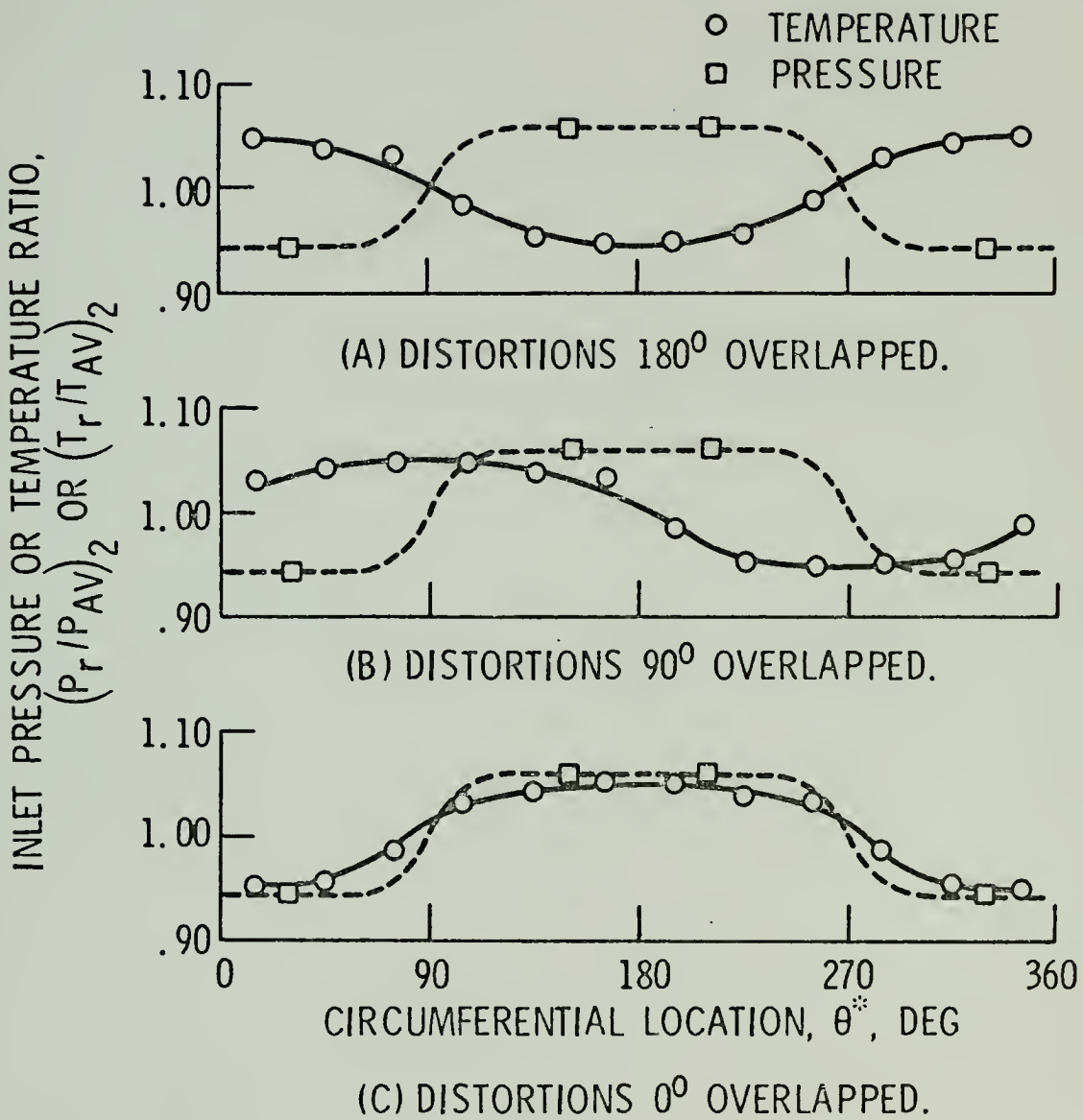

Figure 5. Compressor Inlet Temperature and Pressure Profiles with Combined 180° Extent Pressure and Temperature Distortions (From Ref. 5).

ω_r is small, and there should be only small loss of stall margin. For the 0° overlapped case, Fig. 5(c), $\partial P_t/\partial\theta^*$ and $\partial T_t/\partial\theta^*$ have the same sign, and ω_r is large. The 0° overlapped case should result in large loss of stall margin. Observing Fig. 4, it can be seen that the opposite result was observed experimentally.

III. MODELS OF FLOW WITH PRESSURE AND TEMPERATURE DISTORTION

Effects on the flow field at the face of the compressor when distortions are imposed upstream by screens (pressure) or heating (temperature) will be examined. Table 1 contains a list of influence coefficients for area change (dA/A), heat addition (dh_t/c_pT) and friction ($dC_f/2$) that will be used in this analysis. These influence coefficients are adapted from Shapiro [Ref. 7].

A. PRESSURE DISTORTION

Figure 6 is a schematic of the model used for pressure distortion. The streamline curvature depicted is for graphic purposes, and it is not assumed that the streamtube change actually will be as drawn. The screen is assumed to be of 180° extent (which is consistent with the methods of Ref. 5), and the flow at station 1 is assumed to be uniform. From continuity

$$\dot{m}_{A1} = \dot{m}_{A2} = \rho_1 U_1 A_1 = \text{mass flow rate}$$

or in differential form after logarithmic differentiation

$$d\dot{m} = 0 = \frac{d\rho}{\rho} + \frac{dU}{U} + \frac{dA}{A} \quad .$$

The physical geometry requires that

$$\left(\frac{dA}{A}\right)_A = -\left(\frac{dA}{A}\right)_B \quad . \tag{4}$$

The assumed uniform static pressure distribution requires that

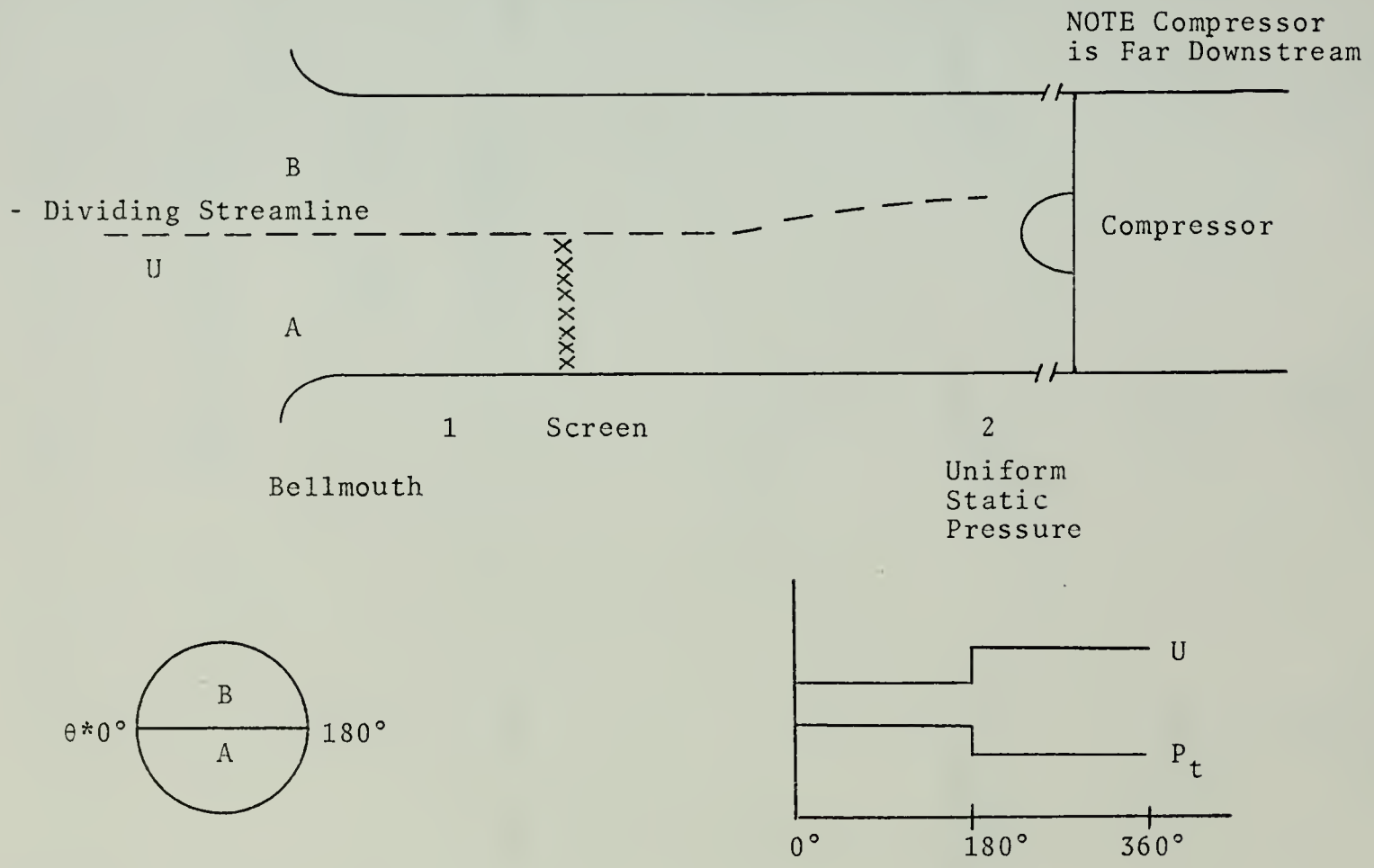

Figure 6. Pressure Distortion Model (Schematic).

	AREA CHANGE $\frac{dA}{A}$	HEAT ADDITION $\frac{d h_t}{c_p T}$	FRICTION $\frac{d C_f}{2}$
$\frac{dU}{U}$	$\frac{1}{M^2 - 1}$	$- \frac{1}{M^2 - 1}$	$\frac{\gamma M^2}{1-M^2}$
$\frac{dp}{p}$	$- \frac{\gamma M^2}{M^2 - 1}$	$\frac{\gamma M^2}{M^2 - 1}$	$- \frac{[1 + M^2 (\gamma - 1)]\gamma M^2}{1 - M^2}$
$\frac{dT_t}{T_t}$	0	$\frac{1}{1 + \frac{\gamma - 1}{2} M^2}$	0

TABLE 1. Influence coefficients for area change, heat addition and friction.

$$\left.\frac{dP}{P}\right)_A = \left.\frac{dP}{P}\right)_B . \tag{5}$$

From Table 1

$$\left.\frac{dP}{P}\right)_B = \frac{-\gamma M^2}{M^2 - 1} \left.\frac{dA}{A}\right)_B \tag{6}$$

$$\left.\frac{dP}{P}\right)_A = \frac{- \gamma M^2}{M^2 - 1} \left.\frac{dA}{A}\right)_A - \frac{[1 + M^2(\gamma-1)]\gamma M^2}{1 - M^2} \frac{dC_f}{2} . \tag{7}$$

Combining Equations (4), (5), (6), and (7) and algebraic

manipulation yields the following relationship for area change:

$$\frac{dA}{A})_A = [1 + M^2 (\gamma - 1)] \frac{dC_f}{4} = - \frac{dA}{A})_B . \qquad (8)$$

Using similar techniques to investigate velocity, it can be shown that

$$\frac{dU}{U})_A = \frac{1}{M^2 - 1} \frac{dA}{A})_A + \frac{\gamma M^2}{1 - M^2} \frac{dC_f}{2} , \qquad (9)$$

and combining Equations (8) and (9) with some simplification reduces to

$$\frac{dU}{U})_A = \left[\frac{M^2(1 + \gamma) - 1}{2(1 - M^2}\right] \frac{dC_f}{2} . \qquad (10)$$

From Table 1

$$\frac{dU}{U})_B = - \frac{1}{1 - M^2} \frac{dA}{A})_B \qquad (11)$$

and the ratio of velocity changes can be expressed as

$$\frac{\frac{dU}{U})_A}{\frac{dU}{U})_B} = \frac{\frac{(\gamma + 1)M^2 - 1}{2} \frac{dC_f}{2}}{\frac{-1}{1 - M^2} \frac{dA}{A})_B}$$

which, using Equation (8), reduces to

$$\frac{\frac{dU}{U})_A}{\frac{dU}{U})_B} = \frac{(\gamma + 1)M^2 - 1}{1 + (\gamma - 1)M^2} = \frac{2.4 M^2 - 1}{1 + 0.4 M^2} = f(M) \qquad (12)$$

for $\gamma = 1.4$.

Equation (8) shows that for all real valued Mach numbers, streamtube A will increase in cross sectional area (the friction coefficient is always positive), and streamtube B must

decrease a like amount as in Equation (4). For subsonic flow, U_{B2} must then be greater than U_{B1}. Equation (12) is finite for all real values of Mach number but changes sign when M = 0.6455. For values of M less than 0.6455, Equation (12) is negative which requires the velocity change in streamtube A to be negative. Conversely when M > 0.6455, $U_{A2} > U_{A1}$. Quantitatively M may be less than 0.6455 although transonic compressors have axial Mach numbers approaching 0.65.

B. TOTAL TEMPERATURE DISTORTION

Figure 7 is a schematic of the total temperature distortion model. The illustrated curvature of the streamtube is for graphic purposes and does not represent an assumed pattern of change. At station 2 the static pressure distribution is assumed to be uniform. This implies that station 2 is far enough ahead of the compressor so that there is no upstream effect of the engine.

Using Table 1

$$\frac{dP}{P})_B = \frac{\gamma M^2}{1 - M^2} \frac{dA}{A})_B \tag{13}$$

$$\frac{dP}{P})_A = \frac{\gamma M^2}{1 - M^2} \frac{dA}{A})_A - \frac{\gamma M^2}{1 - M^2} \frac{dh_t}{c_p T} \quad . \tag{14}$$

Setting Equation (13) equal to Equation (14), because of the uniform pressure assumption, then

$$\frac{dA}{A})_B - \frac{dA}{A})_A = - \frac{dh_t}{c_p T} \quad . \tag{15}$$

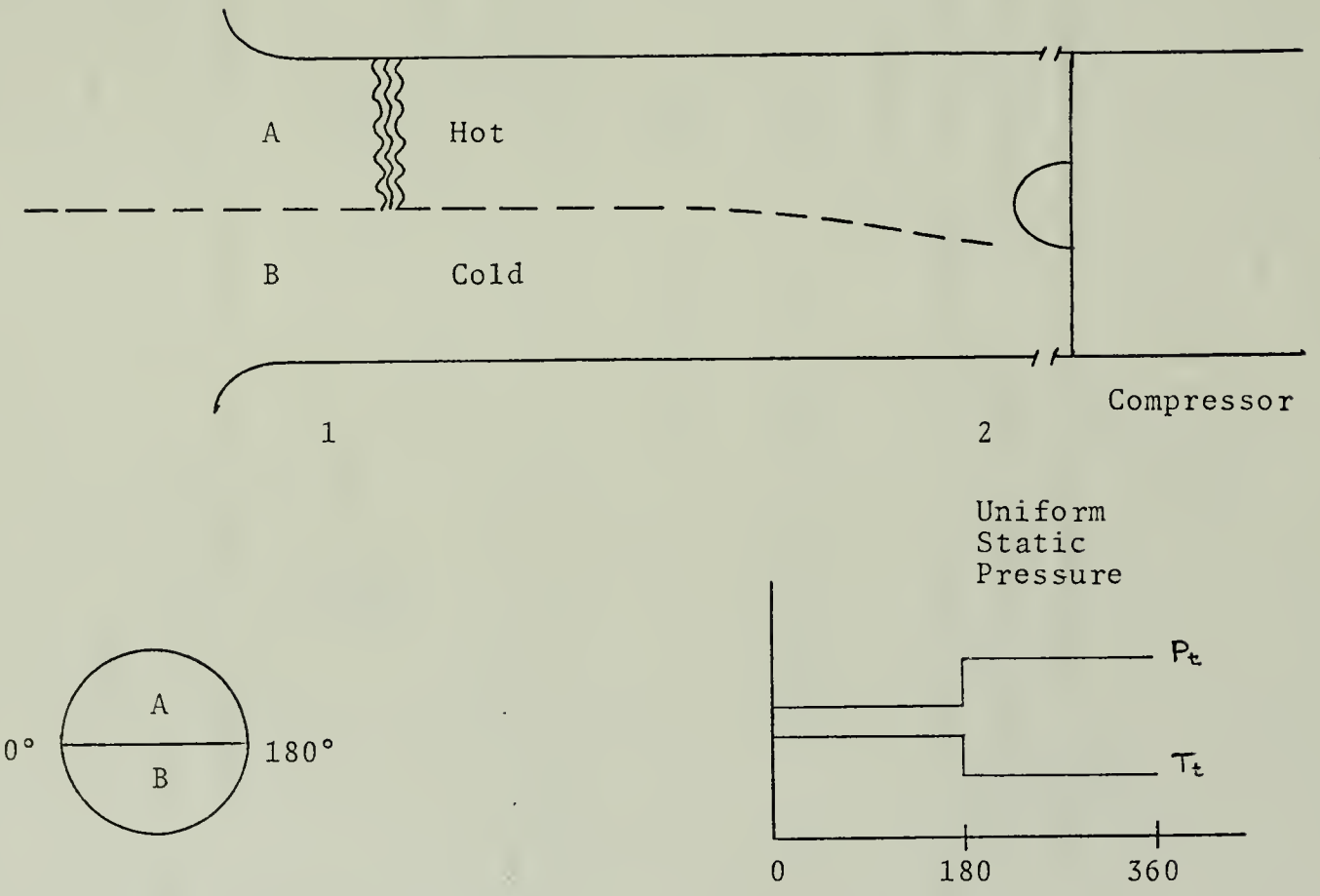

Figure 7. Total Temperature Distortion Model (Schematic)

Since

$$\frac{dA}{A})_B = - \frac{dA}{A})_A ,$$

Equation (15) becomes

$$\frac{dA}{A})_B = - \frac{dA}{A})_A = - \frac{1}{2} \frac{dh_t}{c_p T} \quad . \tag{16}$$

With the addition of heat, $\frac{dA}{A})_B$ decreases and $\frac{dA}{A})_A$ increases; and for subsonic flow, U_{B2} must be greater than U_{B1}.

The effect of heat addition on the velocity is investigated similarly

$$\frac{dU}{U})_A = - \frac{1}{1 - M^2} \frac{dA}{A})_A + \frac{1}{1 - M^2} \frac{dh_t}{c_p T} \tag{17}$$

$$\frac{dU}{U})_B = - \frac{1}{1 - M^2} \frac{dA}{A})_B \quad . \tag{18}$$

Incorporating the streamtube area changes of Equation (16) into Equations (17) and (18), the velocity change is found to be the same for both streamtubes.

$$\frac{dU}{U})_A = \frac{dU}{U})_B = \frac{1}{2(1 - M^2)} \frac{dh_t}{c_p T} \quad . \tag{19}$$

C. COMBINED TEMPERATURE AND PRESSURE DISTORTION

Figure 8 is a schematic of the models used for combined pressure and temperature distortion. Cases will be considered for zero degrees overlap and 180° overlap.

From Table 1 the addition of heat causes a loss of stagnation pressure.

$$\frac{dP_t}{P_t} = \frac{- \gamma M^2/2}{1+\frac{\gamma-1}{2} M^2} \frac{dh_t}{c_p T} = - \frac{\gamma M^2}{2} \frac{dh_t}{c_p T_t} \quad .$$

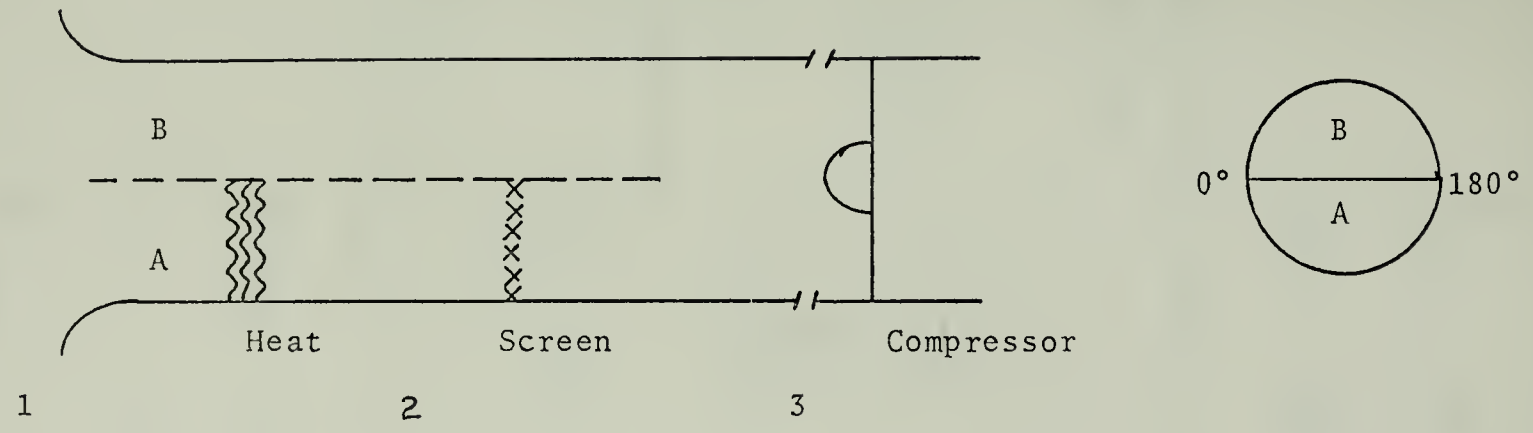

(a) Temperature and Pressure 180° Overlap.

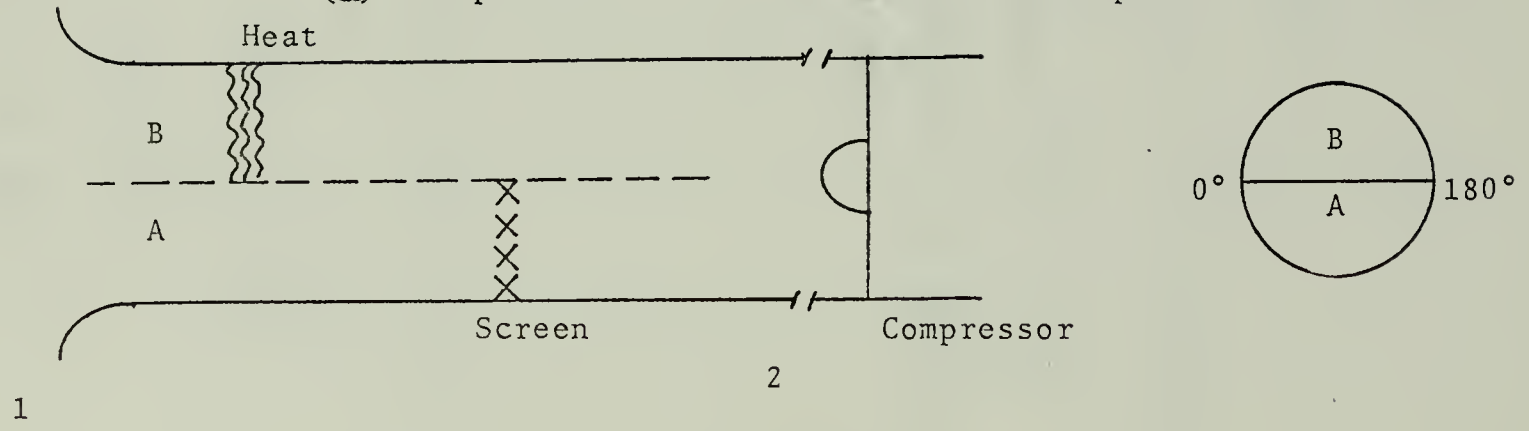

(b) Temperature and Pressure 0° Overlap.

Figure 8. Combined Temperature and Pressure Distortion Model for 0° and 180° Overlap.

In the case of 0° overlap

$$\frac{dP_t}{P_t})_A = -\frac{\gamma M^2}{2} dC_f \qquad (20)$$

$$\frac{dP_t}{P_t})_B = -\frac{\gamma M^2}{2} \frac{dh_t}{c_p T_t} \quad . \qquad (21)$$

The net area change of streamtube A is, using Equations (8) and (16),

$$\frac{dA}{A})_{ANET} = [1 + (\gamma-1) M^2] \frac{dC_f}{4} - \frac{1}{2} \frac{dh_t}{c_p T} \quad . \qquad (22)$$

To obtain results for a specific case, let us assume that the heat and screens are such that

$$\frac{dC_f}{2} = \frac{1}{2} \frac{dh_t}{c_p T_t} \quad .$$

Consequently

$$\frac{dP_t}{P_t})_A = \frac{dP_t}{P_t})_B \quad .$$

Equation (22) in terms of T_t and introducing $dC_f/2$ in terms of heat becomes

$$\frac{dA}{A})_{ANET} = \frac{[1 + (\gamma-1) M^2]}{2} \left[\frac{1}{2} \frac{dh_t}{c_p T_t}\right] - \frac{1}{2} \left[1 + \frac{\gamma-1}{2} M^2\right] \frac{dh_t}{c_p T_t}$$

$$\frac{dA}{A})_{ANET} = -\frac{1}{4} \frac{dh_t}{c_p T_t} = -\frac{1}{2} \frac{dC_f}{2} \quad . \qquad (23)$$

For velocity change in streamtube A,

$$\frac{dU}{U})_A = \frac{1}{1 - M^2} \frac{dA}{A})_{ANET} + \frac{\gamma M^2}{1 - M^2} \frac{dC_f}{2},$$

and incorporating Equation (23) simplifies to

$$\frac{dU}{U})_B = \frac{1 + 2\gamma M^2}{(1 - M^2)\ 2} \frac{dC_f}{2} . \tag{24}$$

In streamtube B,

$$\frac{dU}{U})_B = \frac{-1}{1 - M^2} \frac{dA}{A})_{BNET} + \frac{1}{1 - M^2} \frac{dh_t}{c_p T}$$

$$\frac{dU}{U})_B = \frac{1}{1 - M^2} \frac{dA}{A})_{ANET} + \frac{1}{1 - M^2} \frac{dh_t}{c_p T}$$

$$\frac{dU}{U})_B = \frac{3/2 + (\gamma - 1)M^2}{1 - M^2} \frac{dC_f}{2} . \tag{25}$$

The ratio of velocity changes in the two streamtubes (for $\gamma = 1.4$) is

$$\frac{\frac{dU}{U})_B}{\frac{dU}{U})_A} = \frac{1.5 + 0.4\ M^2}{0.5 + 1.4\ M^2} = f(M) \tag{26a}$$

Examination of Equation (26a) shows that the velocity in streamtube B is higher for all subsonic values of M. Recall that this result is for the specific case of equal total pressure in streamtubes A and B which resulted from the arbitrary relation of $dC_f/2 = 1/2 \cdot dh_t/c_p T_t$.

For the case of 180° overlap the same method of development is used. Figure 8(a) is the model used, and there are three stations illustrated for the purpose of adding the solutions of each distortion. Assume that static pressure

is uniform at stations 2 and 3. Adding Equations (19) and (10) and again considering the specific case of

$$\frac{dC_f}{2} = \frac{1}{2} \frac{dh_t}{c_p T_t}$$

the velocity change in streamtube A is

$$\left(\frac{dU}{U}\right)_A = \frac{dC_f}{4(1-M^2)} \quad (1 + 2\gamma M^2) \quad .$$

For streamtube B, using Table 1, Equations (8), (16), and (19) the velocity change is

$$\left(\frac{dU}{U}\right)_B = \frac{dC_f}{4(1-M^2)} [3 + 2M^2(\gamma-1)]$$

and the ratio of velocity changes is, for $\gamma = 1.4$,

$$\frac{\left(\frac{dU}{U}\right)_A}{\left(\frac{dU}{U}\right)_B} = \frac{1 + 2M^2}{3+2M^2(\gamma-1)} = \frac{1 + 2.8M^2}{3 + 0.8M^2} = f(M) \quad . \qquad (26b)$$

Examination of Equation (26b) shows that the velocity in streamtube B is always higher than the velocity of streamtube A. For the case of 180° overlap of distortions, the total pressure will not remain equal in both streamtubes as in the case of 0° overlap. In the case of 180° overlap, the change in total pressure for the distorted streamtube (A) will be

$$-2\gamma M^2 \frac{dC_f}{2}$$

for this specific case of

$$\frac{dC_f}{2} = \frac{1}{2} \frac{dh_t}{c_p T_t} \quad .$$

Total pressure will remain constant in the undistorted streamtube (B).

D. HEAT ADDITION AT SMALL MACH NUMBERS

Using the temperature distortion model of Figure 9, the effects of heat addition on the flow field will be made more restrictive by limiting the entering Mach number to very small (near zero) values. This is accomplished by placing the burner outside the bellmouth, where velocities are small. This analysis also models the tests by NASA reported in Ref. 5. An energy balance at stations 1 and 2, assuming adiabatic conditions between these stations, gives

$$\dot{m}_A(c_p T_{A1} + \tfrac{1}{2} U_{A1}^2) + \dot{m}_B(c_p T_{B1} + \tfrac{1}{2} U_{B1}^2) =$$

$$\dot{m}_A(c_p T_{A2} + \tfrac{1}{2} U_{A2}^2) + \dot{m}_B(c_p T_{B2} + \tfrac{1}{2} U_{B2}^2) \quad . \qquad (27)$$

Note that station 1 is immediately downstream from the burner. For streamtubes A and B then

$$c_p T_{A1} + \tfrac{1}{2} U_{A1}^2 = c_p T_{A2} + \tfrac{1}{2} U_{A2}^2 = c_p T_{tA} \qquad (28)$$

and

$$c_p T_{B1} + \tfrac{1}{2} U_{B1}^2 = c_p T_{B2} + \tfrac{1}{2} U_{B2}^2 = c_p T_{tB} \quad . \qquad (29)$$

Assume uniform P at stations 1 and 2, $\dot{m}_A = \dot{m}_B$ and isentropic flow for streamtubes A and B between stations 1 and 2. With the previous assumption of small Mach number, conditions at station 1 are specified. The stagnation pressure for both streamtubes at either station 1 or 2 equals the ambient

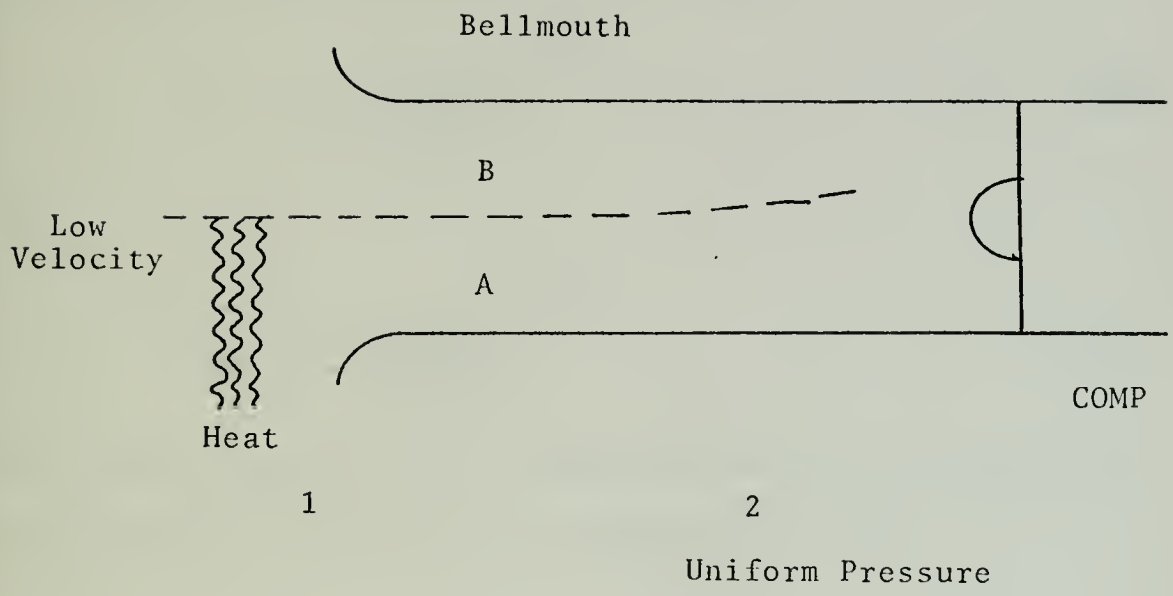

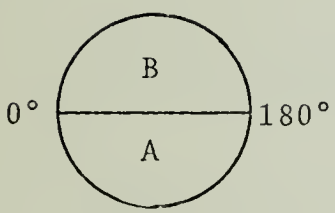

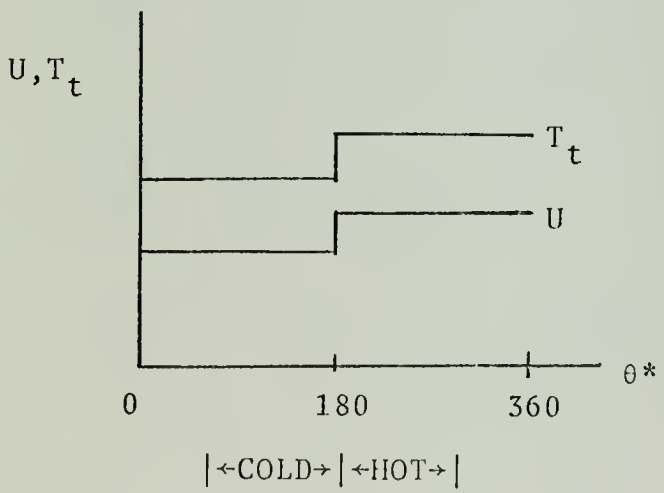

Figure 9. Temperature Distortion Model for Heat Addition at Low Mach Number.

pressure. Static pressure for both streamtubes is equal at station 1. Due to heat addition $T_{tA} > T_{tB}$. The following isentropic relationships now can be used:

$$T_{A2} = T_{tA} \left(\frac{P_{A2}}{P_{tA1}} \right)^{\frac{\gamma-1}{\gamma}} \tag{30}$$

and

$$T_{B2} = T_{tB} \left(\frac{P_{B2}}{P_{tB1}} \right)^{\frac{\gamma-1}{\gamma}} . \tag{31}$$

Using Equations (30), (31) with (28) and (29) will give the relationship of velocity for streamtubes A and B

$$U_{A2}^2 = 2c_p T_{tA} \left[1 - \left(\frac{P_2}{P_t} \right)^{\frac{\gamma-1}{\gamma}} \right]$$

$$U_{B2}^2 = 2c_p T_{tB} \left[1 - \left(\frac{P_2}{P_t} \right)^{\frac{\gamma-1}{\gamma}} \right]$$

$$\frac{U_{A2}^2}{U_{B2}^2} = \frac{T_{tA}}{T_{tB}} . \tag{32}$$

Since

$$\left(\frac{P}{P_t} \right)_A = \left(\frac{P}{P_t} \right)_B = f(\gamma, M)$$

and for hydrogen (fuel for burner in NASA test of Ref. 5) oxidized in excess air, $\gamma_A \simeq \gamma_B$, then $M_{A2} = M_{B2}$. (33)

Investigating the area change at 2 with the same assumptions

$$\rho AU)_{B2} = \rho AU)_{A2} \Longrightarrow \frac{A_{A2}}{A_{B2}} = \frac{P_{B2}}{P_{A2}} \frac{T_{A2}}{T_{B2}} \frac{\sqrt{T_{tB}}}{\sqrt{T_{tA}}}$$

$$\frac{M_{A2}^2}{M_{B2}^2} = \frac{U_{A2}^2}{U_{B2}^2} \frac{T_{B2}}{T_{A2}} = 1$$

and using Equation (32)

$$\frac{A_{A2}}{A_{B2}} = \frac{\sqrt{T_{tA}}}{\sqrt{T_{tB}}} \quad . \tag{34}$$

Equation (34) is restrictive in that the assumptions limit it to the case of equal mass flow in streamtubes A and B. However, parallel compressor theory uses a mass-weighted sum of subcompressors to determine the operating point of a distorted compressor, so in the case of 180° sector distortion this assumption is not unreasonable.

IV. COMPARISON OF FLOW MODELS WITH VORTICITY THEORY FOR TEMPERATURE DISTORTION

The analysis of Section III(B), total temperature distortion, shows that the velocities of the two streamtubes are the same, thus making the radial vorticity zero. Setting ω_r in Equation (3) equal to zero and solving for $\partial P_t/\partial\theta^*$ yields the following relationship:

$$\frac{RT_t}{rP_tU_z}\frac{\partial P_t}{\partial\theta^*} = -\frac{c_p}{rU_z}\frac{\partial T_t}{\partial\theta^*}\left[\frac{\frac{\gamma-1}{2}M^2}{1+\frac{\gamma-1}{2}M^2}\right] .$$

Simplifying and changing T to T_t gives

$$RT_t\frac{dP_t}{P_t} = -c_p\,dT_t\,\frac{\gamma-1}{2}M^2$$

$$\frac{dP_t}{P_t} = -\frac{\gamma-1}{2}\frac{dh_t}{RT_t}M^2\frac{c_p}{c_p}$$

and since $R/c_p = (\gamma-1)/\gamma$

$$\frac{dP_t}{P_t} = -\frac{\gamma-1}{2}\frac{c_p}{R}\frac{dh_t}{c_pT_t}M^2 = -\frac{\gamma M^2}{2}\frac{dh_t}{c_pT_t} . \qquad (35)$$

Equation (35) is equivalent to the influence coefficient of Table 1, thus verifying vorticity for this case.

For the case of heat addition at low Mach number, a more subjective comparison must be made. Equation (3) simplified for temperature distortion only shows

$$\omega_r = \frac{c_p}{RU_z} \frac{\partial T_t}{\partial \theta^*} \left\{ \frac{\frac{\gamma-1}{2} M^2}{\frac{\gamma-1}{2} M^2 + 1} \right\} \quad . \qquad (36)$$

All values in the right hand side of Equation (36) are always positive with the exception of the circumferential total temperature gradient. For the velocity profile shown in Figure 9, ω_r is positive when $\theta^* = 180°$ and $\partial T_t/\partial \theta^*$ is also positive. A similar comparison at $\theta^* = 0°$ also shows algebraic agreement in that ω_r and the total temperature gradient are both negative.

V. EXTENDED MODEL TO ACCOUNT FOR COMPRESSOR INFLUENCE

A. PARALLEL COMPRESSOR MODEL

Reference 5 employs the parallel compressor model as a method of predicting the effects of distortion on stall pressure ratios. Figure 10 shows a schematic of the parallel compressor model with some of the assumptions used. Figure 11 shows the predicted stall points of the compressor for various pressure and temperature distortions using this model. Figures 12 and 13 show the profiles of static pressure, total pressure and total temperature at the compressor inlet and outlets for both pressure and temperature distortion. From Figure 12 it can be seen that static pressure is not uniform at the face (inlet) of the compressor. This was one of the assumptions used in the development of Section III of this paper. The development of an extended model in this section will consider the effects of non-uniform pressure profiles.

B. PRESSURE RATIO EQUATION

Hill and Peterson [Ref. 8] derive a compressor pressure ratio equation that predicts the total pressure ratio (Π_c) across an axial compressor stage as

$$\Pi_c = \left[1 + \frac{(\Omega r)^2}{c_p T_{t1}} \left(1 - \frac{\tan \beta 2}{\tan \beta 1} \right) \right] \qquad (37)$$

where the subscripts 1 and 2 refer to stations before and

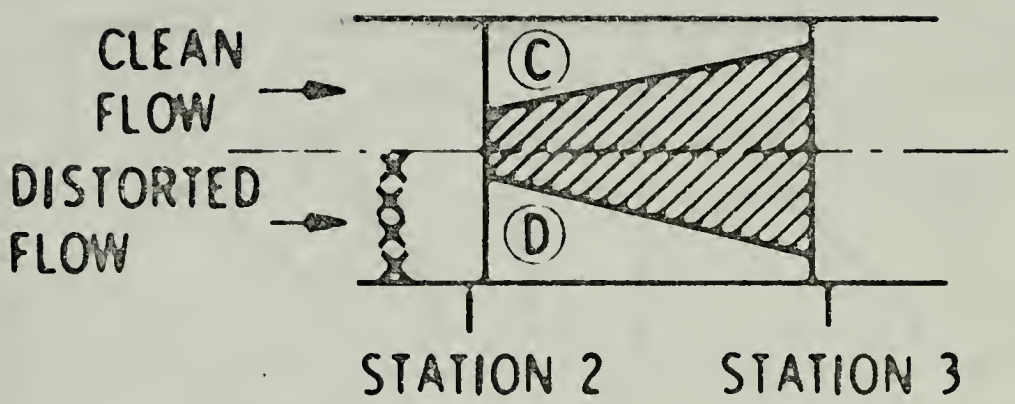

1. SECTORS C AND D ARE CONSIDERED AS INDEPENDENT PARALLEL COMPRESSORS
2. BOTH SECTORS FOLLOW SAME MAP AS UNDISTORTED COMPRESSOR
3. NO CROSSFLOW BETWEEN PARALLEL COMPRESSORS
4. BOTH EXIT TO A COMMON STATIC PRESSURE

Figure 10. Parallel Compressor Model (From Ref. 5)

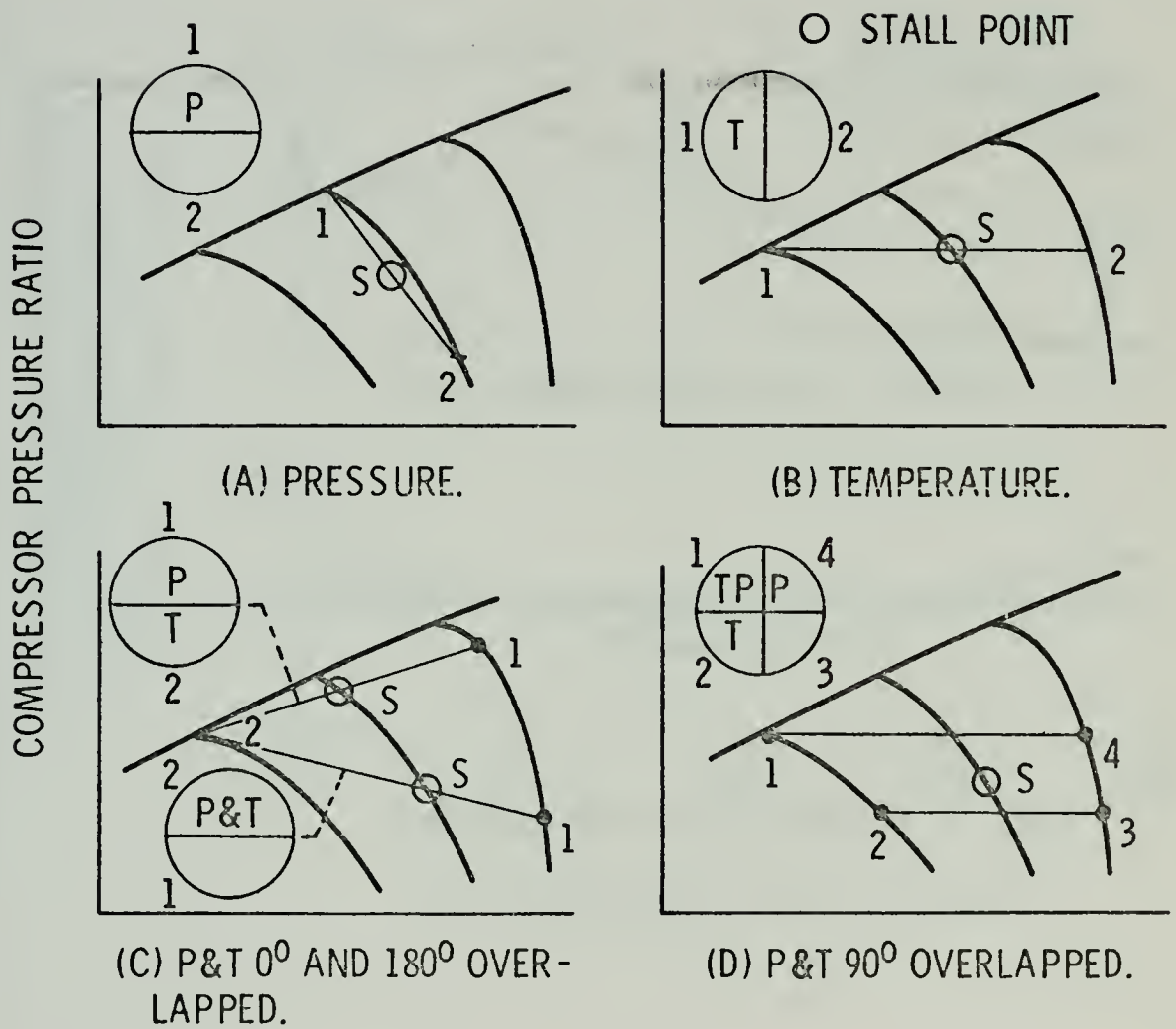

Figure 11. Application of Parallel Compressor Model to Predict Stall Points (From Ref. 5).

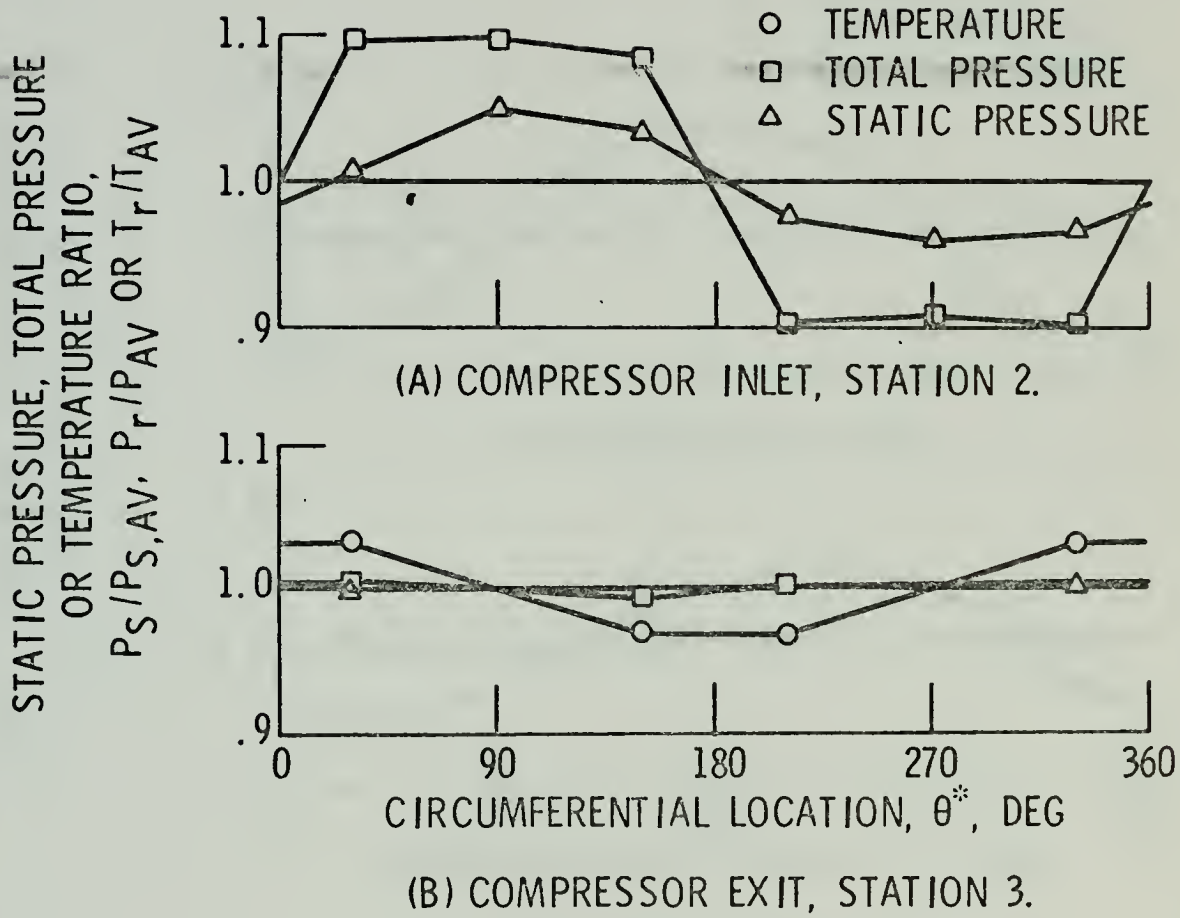

Figure 12. Compressor Temperature and Pressure Profiles with 180° Circumferential Temperature Distortion (From Ref. 5).

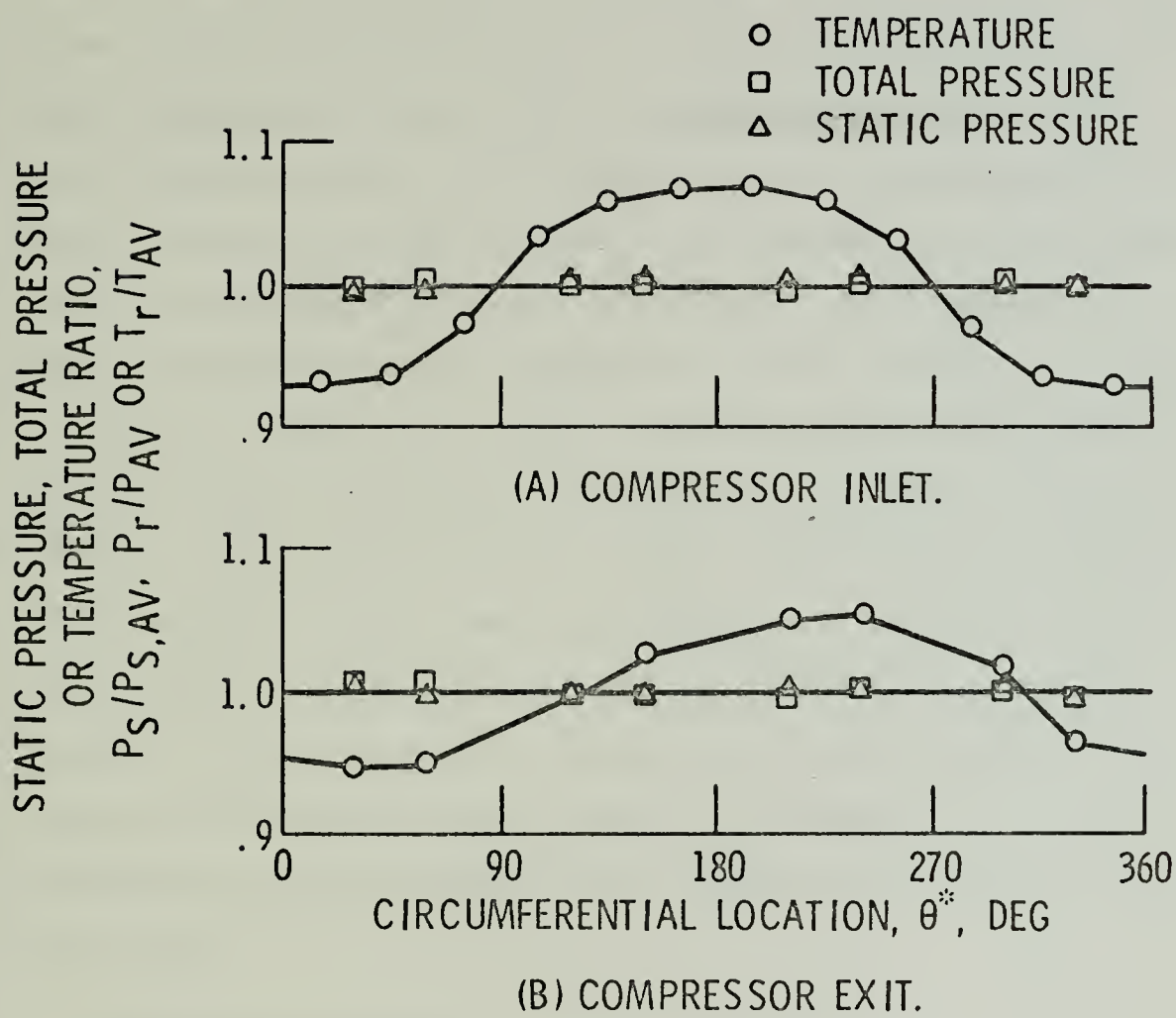

Figure 13. Compressor Temperature and Pressure Profiles with 180° Circumferential Temperature Distortion (From Ref. 5).

after the compressor stage. Figure 14 shows the relationship of the angles β_1 and β_2 with a compressor blade row at wheel speed Ωr. For flow in unstalled cascades of high solidity (ratio of blade chord length to blade spacing in the cascade), the exit angle β_2 is relatively constant with changes of β_1. Blade loading is a function of, or can be correlated to, $\Delta\beta$. If $\beta_2 \simeq$ constant, then β_1 has a significant effect on the stall characteristics of a cascade. Consider Equation (37) with a fixed Π_c and wheel speed. An increase in temperature must be accompanied by an increase in β_1. An increase in β_1 can be obtained only by a decrease in axial velocity. This is shown in Figure 15. Figure 11 shows that parallel compressor theory substantiates the decrease in axial velocity for this case since corrected weight flow is proportional to axial velocity. The model of Section III.D. shows a velocity profile reversed from the results of this section; see Figure 9. An assumption of Section III.D. was uniform static pressure at the downstream station. The model in fact precluded any upstream effect of the compressor itself on the flow field.

C. PRESSURE DISTORTION

Figure 16 illustrates the profiles of static and total pressure, static and total temperature and axial velocity as derived from the models of Section III and as measured at the face of the compressor during the NASA tests of Ref. 5. Flow properties at the constant-static-pressure station

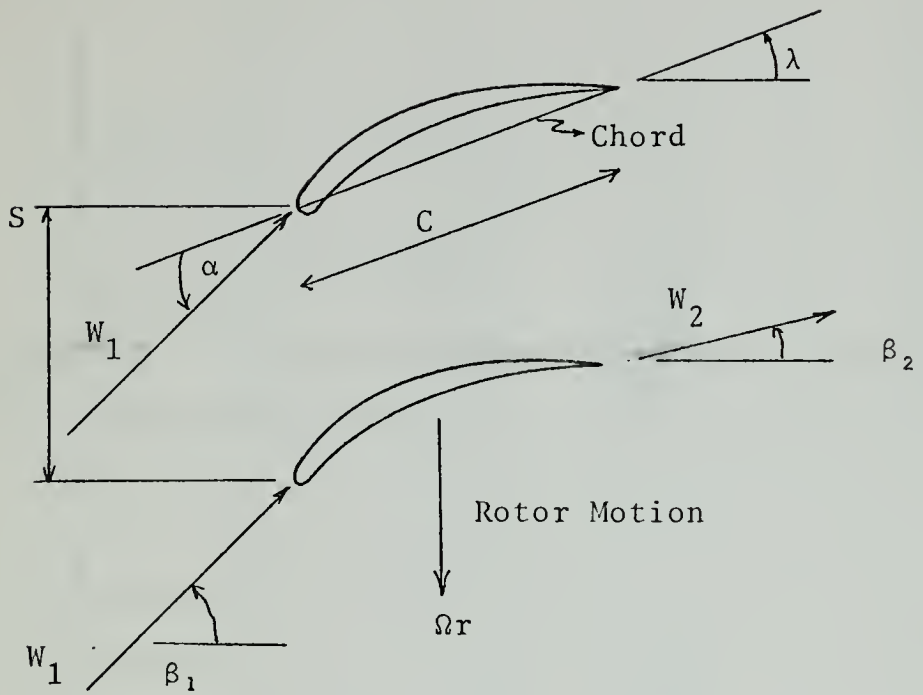

Figure 14. Cascade Geometry for Compressor Rotor.

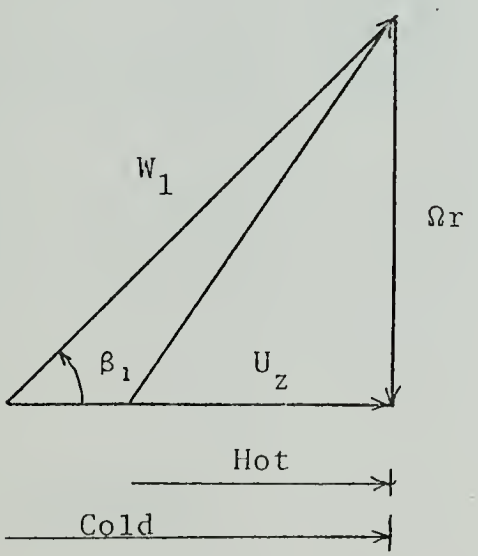

Figure 15. Effects of Temperature on Axial Velocity.

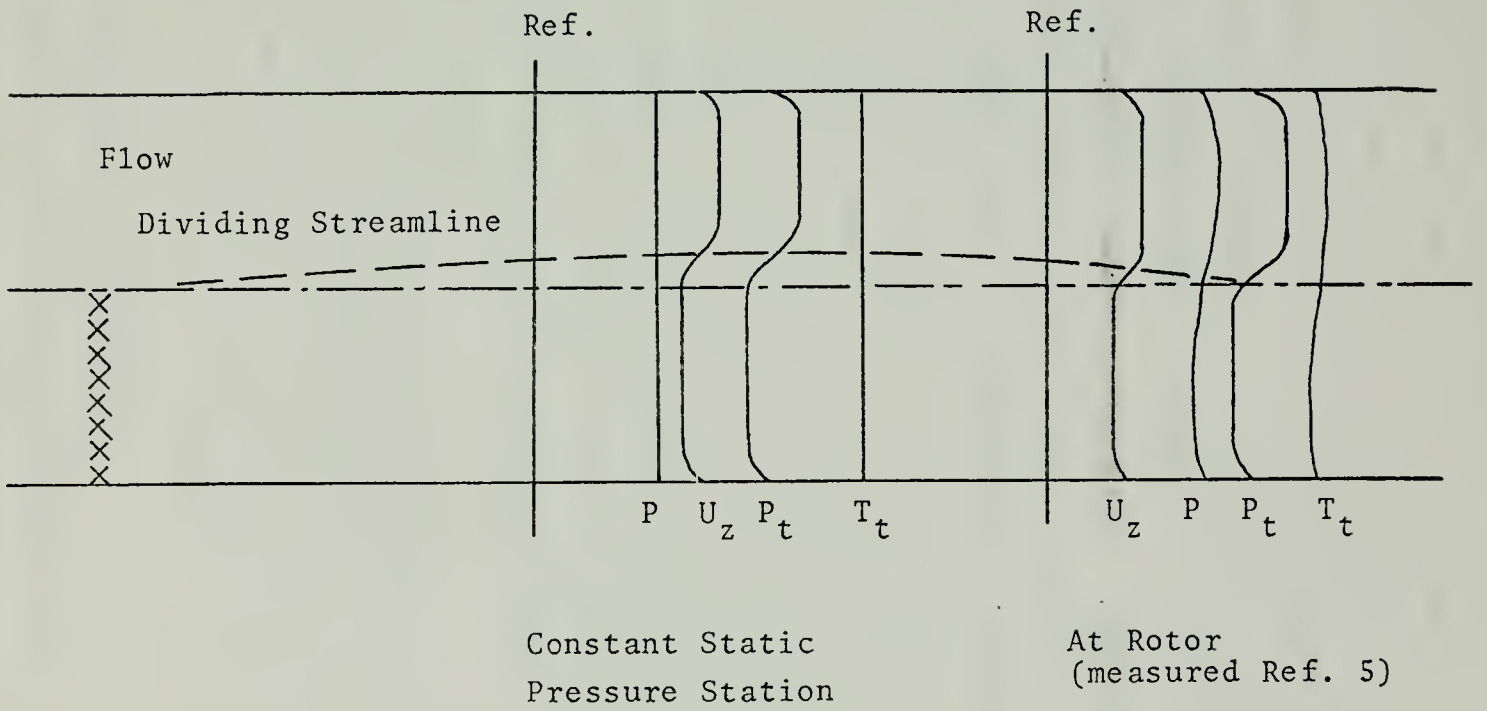

Figure 16. Derived and Measured Profiles of P, P_t, U, T_t for Pressure Distortion.

agree with those illustrated by Figure 6. According to Figure 12, the static pressure increases in the high-P_t streamtube and decreases in the low-P_t streamtube. The flow decelerates in the high-P_t streamtube and vice-versa for low-P_t streamtube. Also the area of the high-P_t streamtube of Figure 6 must increase.

The screen creates a vorticity sheet which is convected into the compressor. This sheet separates the high-P_t and low-P_t streamtubes. As predicted by Helmholtz's vorticity laws, the vortex sheet is a flow feature which persists once it is created [Ref. 9]. The vortex sheet decays by means of viscous forces. Figure 17 shows a model that uses a "bent vortex sheet" associated with the change of velocity and streamtube area for pressure distortion. Specific points (A, B, C, D) in relation to this vortex sheet are indicated, and the change in axial velocity at these points is also shown in Figure 17.

Due to bending of the vortex sheet, the flow acquires a U_θ component in the direction of rotor motion at points A and B and a U_θ opposed to rotor motion at points C and D of Figure 17. This has an influence on β_1 as discussed later.

D. TEMPERATURE DISTORTION

Figure 18 shows the flow properties at three stations: immediately downstream of the burner, at a constant-static-pressure location within the duct and at the rotor inlet station. The flow properties at the constant-static-pressure

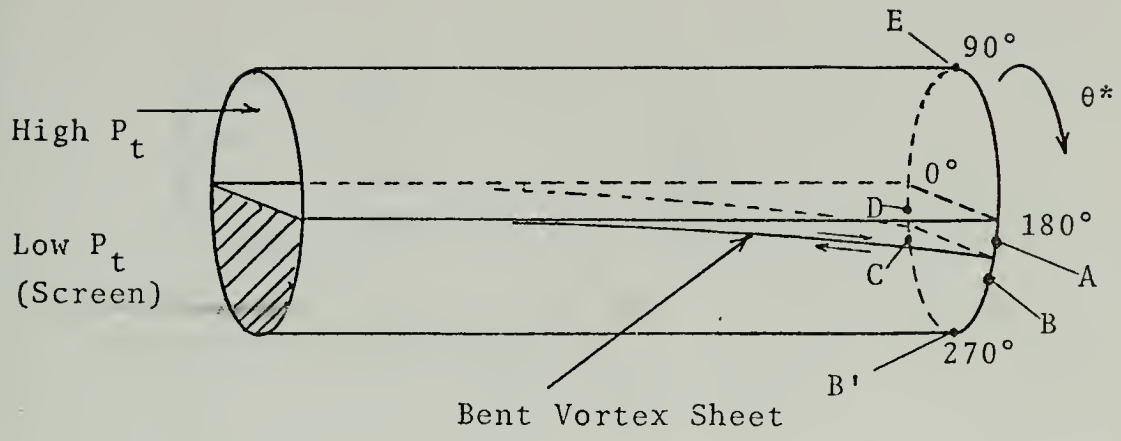

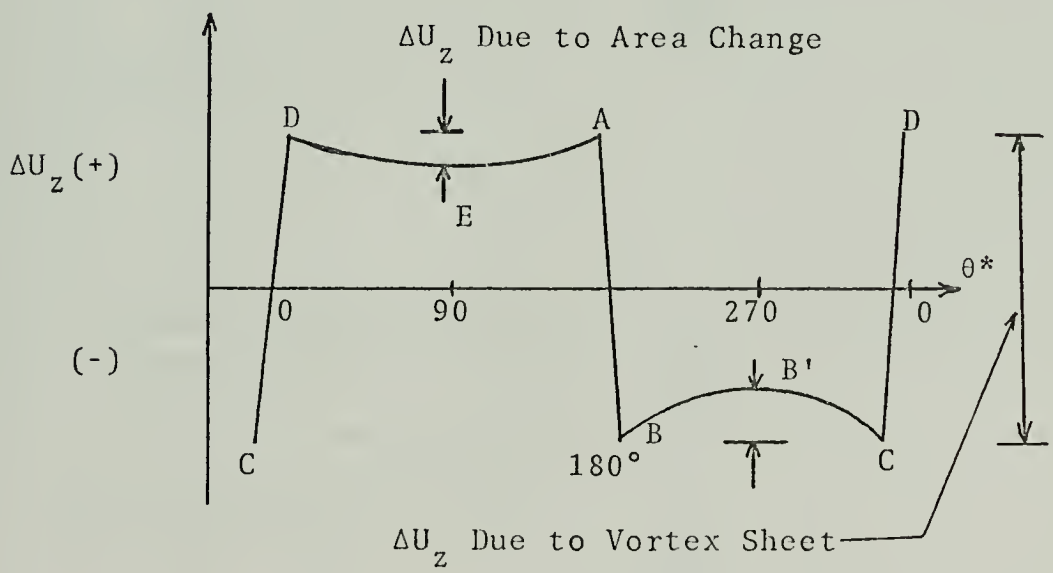

Figure 17. Bent Vortex Model for Pressure Distortion.

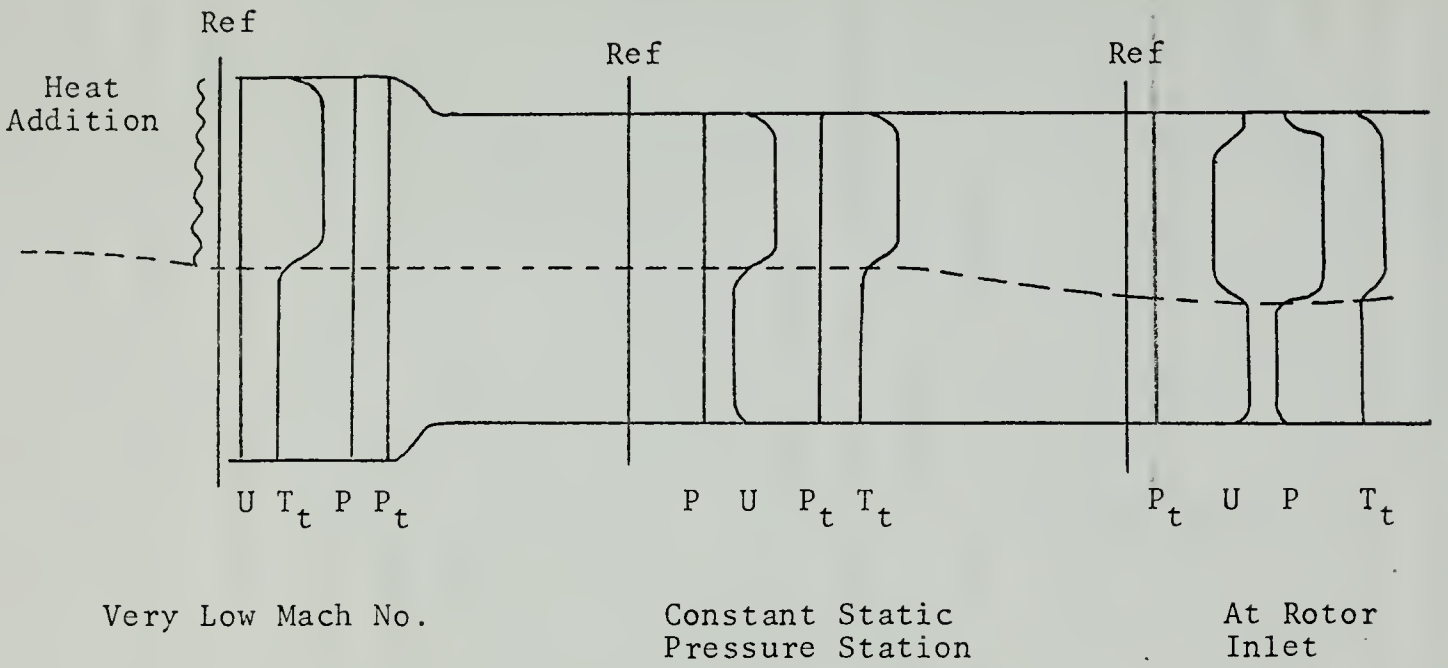

Figure 18. Temperature Distortion with Zero Pressure Distortion.

station within the duct agree with Figure 9 of Section III and figure 13(a).

To determine the upstream influence of the compressor, focus attention on Figure 11(b) which is the parallel compressor model matching Figure 18. The hot streamtube, identified as 1 in Figure 11(b), has sharply reduced corrected weight flow. This implies low axial velocity compared with the cold streamtube, number 2 in Figure 11(b). Consequently, the velocity profile reverses from fast in the hot streamtube at the constant-static-pressure station to slow in the hot streamtube at the rotor. This reversal is attributable to upstream influence of the compressor. The original vorticity sheet generated by heat addition remains. The static pressure is not uniform at the rotor, which was an essential element of the models of Section III. The effect of the compressor must be to change the areas of the streamtubes by an increased corrected weight flow in the undistorted streamtube. Figure 19 shows the bent vortex sheet as applied to the temperature distortion model and the velocity changes at the rotor.

E. EFFECTS OF THE BENT VORTEX SHEET ON ROTOR BLADE INCIDENCE ANGLE

Carta and Adamczyk [Ref. 10] postulate that it is not possible to prescribe the conditions at the compressor face *a priori* on the basis of upstream distortion profiles alone. As discussed in Ref. 10 the upstream conditions are strongly dependent on the presence of the blade row itself. Carta and

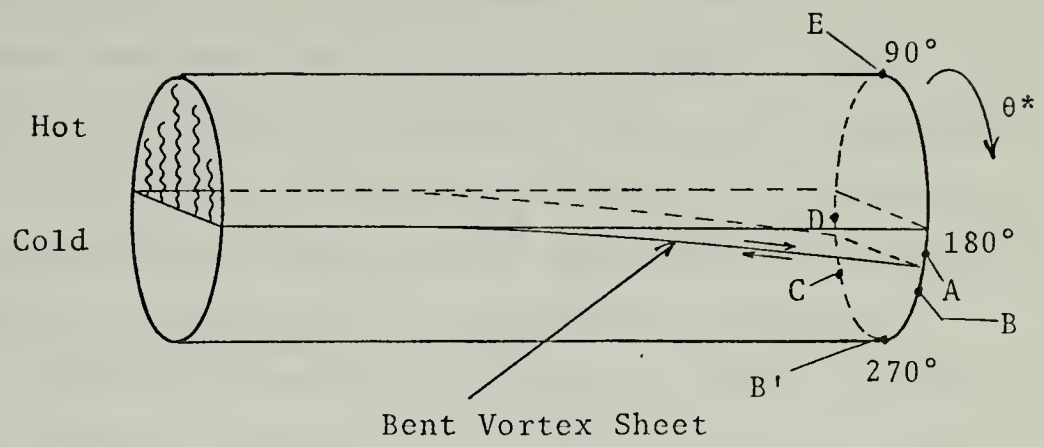

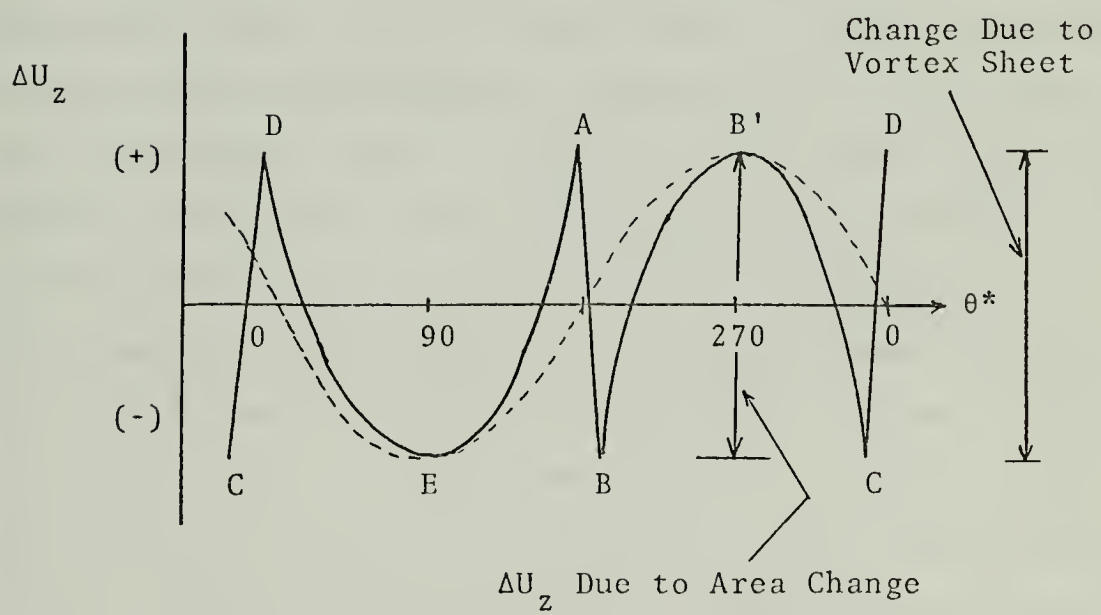

Figure 19. Bent Vortex Model for Heat Addition.

Adamczyk present a graphic comparison of angle of incidence distribution as it differs immediately behind the distortion screen (upstream) from that at the blade row inlet. This angle of incidence distribution of Ref. 10 is compared in Fig. 20 with a semi-quantitative analysis of inlet flow angle based on the bent vortex sheet model for pressure distortion. This analysis is discussed in Appendix B.

There are no measured or predicted angle of incidence distributions available for comparison with the temperature distortion model. However, the encouraging agreement in the case of pressure distortion prompts a similar analysis of temperature distortion. Figure 19 shows the change in axial velocity at the points A, B, B', C, D and E, and Figure 21 shows the change in U_θ at these points. A semi-quantitative analysis similar to Appendix B gives the inlet flow angle (β_1) distribution shown in Figure 22. The area above the nominal clean inlet value of β_1 contributes to stall. The large angles of β_1 in Figure 22 lead the distorted flow sector somewhat, but the majority of the high blade loading due to large values of β_1 lies in the distorted sector. Observing Figure 11(b), it can be seen that the compressor with distorted flow stalls first, which gives qualitative verification of the bent vortex model for temperature distortion.

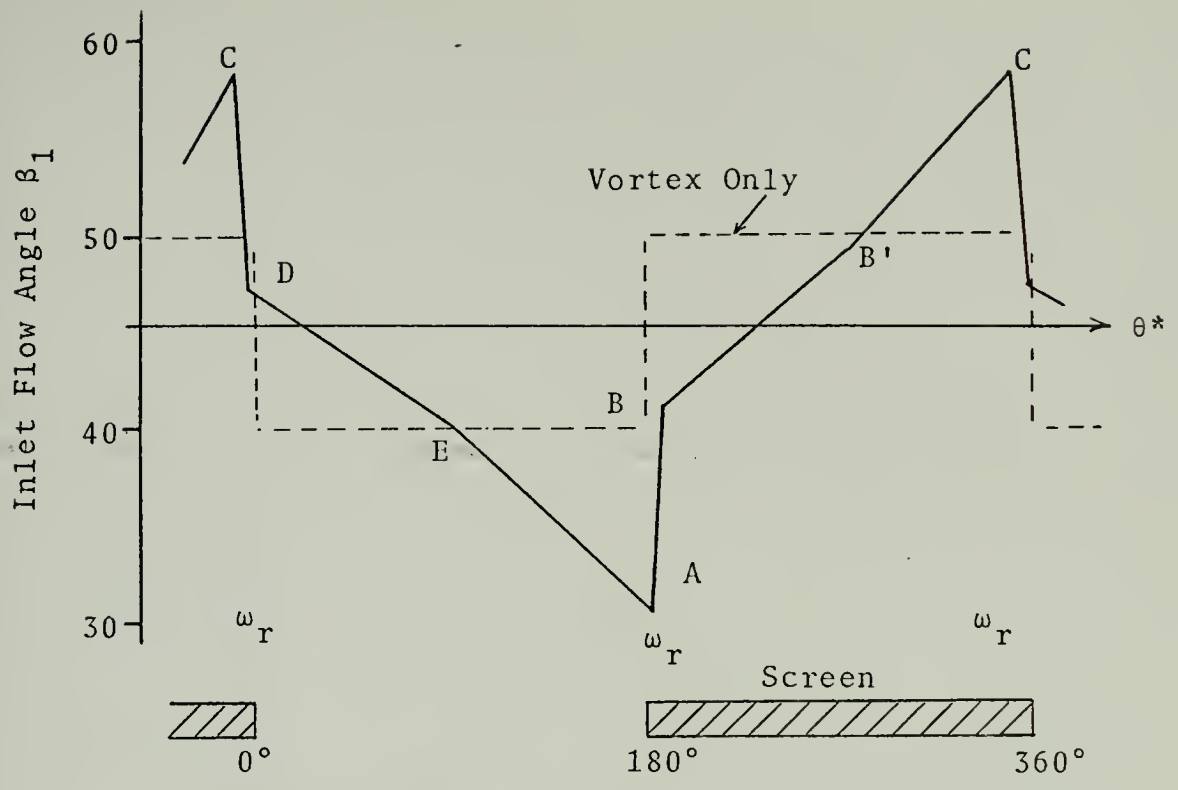

(a) Inlet Flow Angle Distribution vs θ*.

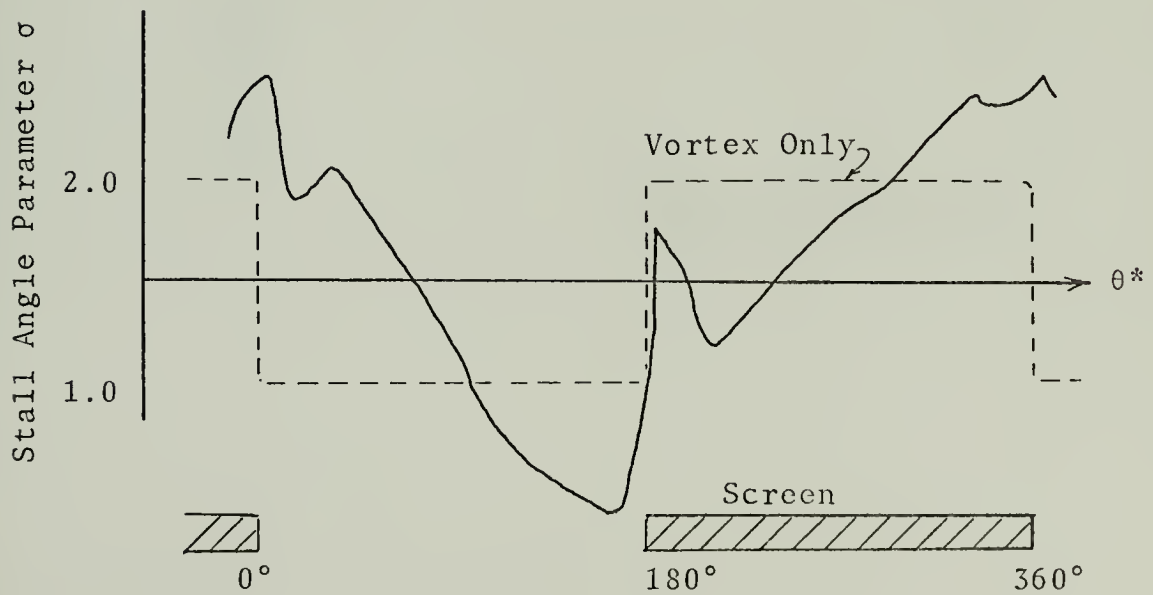

(b) Stall Angle Parameter vs θ* (From Ref. 10)

Figure 20. Effects of Pressure Distortion on Inlet Flow Using Bent Vortex Model.

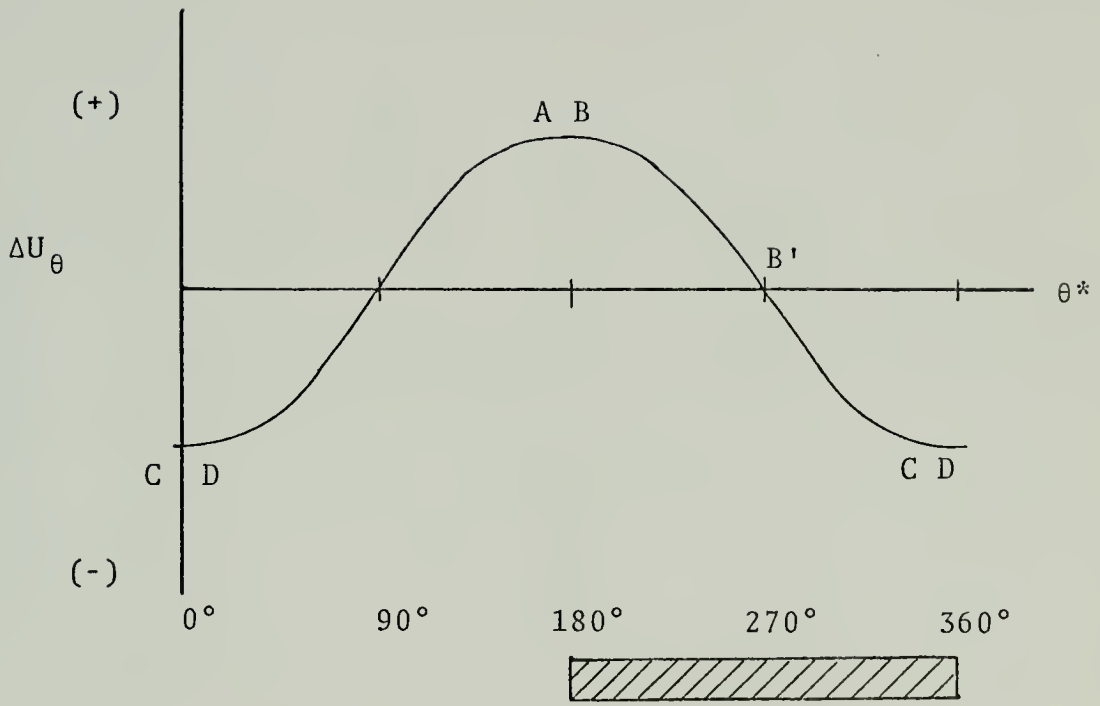

Figure 21. Tangential Velocity Distribution Due to Curvature of Vortex Sheet.

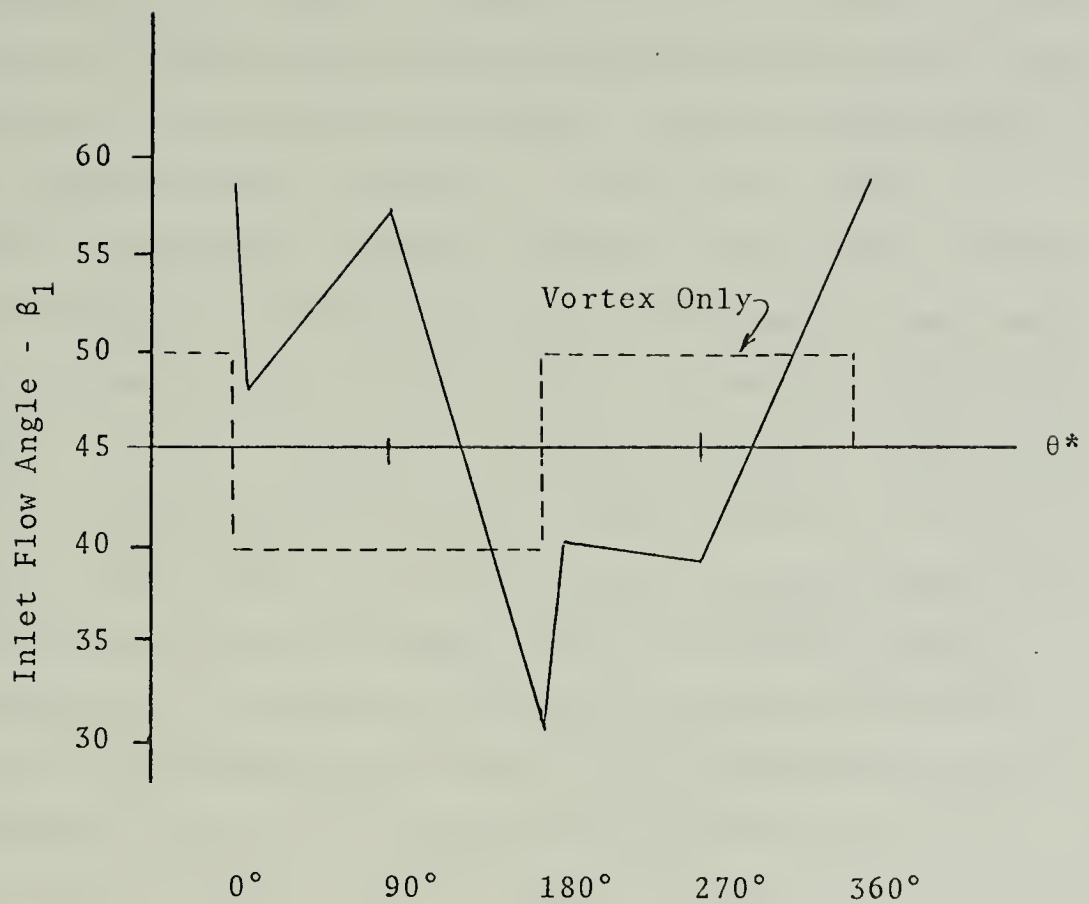

Figure 22. Inlet Flow Angle Distribution for Temperature Distortion Using Bent Vortex Model.

VI. DISTORTION INDEX FORMULATION

The results of Section V suggest an index to predict compressor instability or stall that combines total pressure and radial vorticity. Figure 21 indicates that the area experiencing the highest values of inlet flow angle are those that also would experience positive radial vorticity. Since there are existing data and digital computer programs [Ref. 3] that compute radial vorticity as well as ΔP_t, then it is easy to search the compressor face for these values. There are several possibilities for processing these values, once they are calculated, into an index. One method would be to compare the sum of radial vorticity and ΔP_t for a specified sector (percentage of compressor face area) with a critical value. Since there is no known critical value, another approach that eventually might lead to a critical value is recommended. In Figure 23 the total pressures across the face of the compressor are shown. $\bar{P}_t$ is the average total pressure. If $\bar{P}_t - P_t$ is positive, then the effect is to increase the blade loading as shown in Figure 20. Positive radial vorticity also increases blade loading as shown in Figure 20(a), and as in Refs. 1-3 and 6. The most significant effect on compressor instability or stall would be the largest value of ΔP_t and radial vorticity. The pressure change can be normalized with $\bar{P}_t$, and an index can be formulated by summing, over a sector, the combined values of ΔP_t and ω_r.

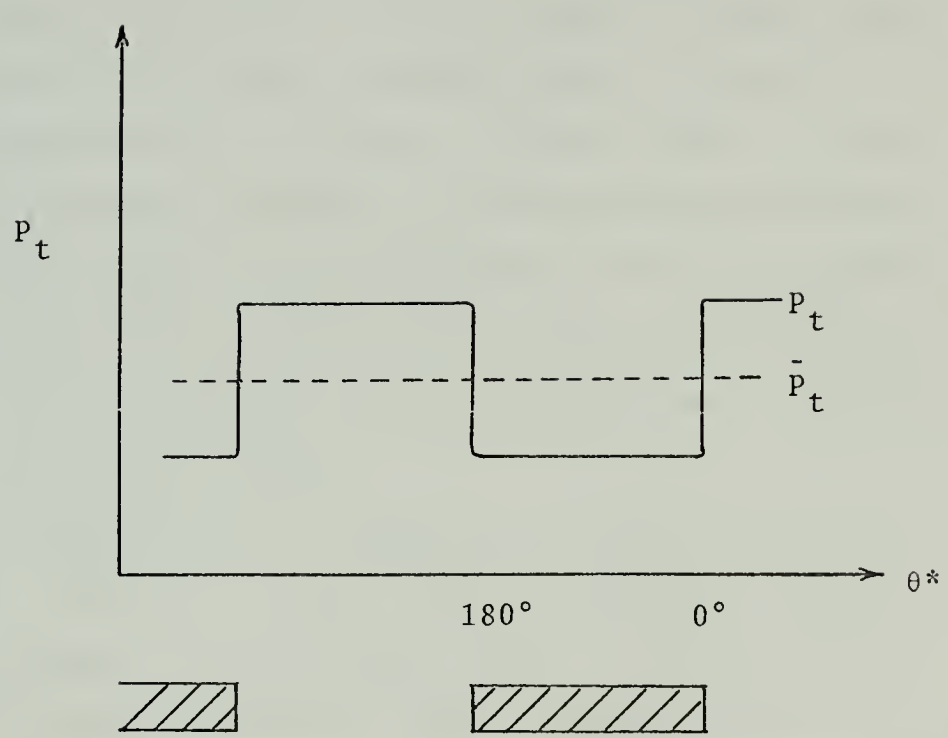

Figure 23. Total Pressure Distribution at the Compressor Face.

$$\text{INDEX} = \sum_{i=1}^{k} (\Delta P_{t_i} + \omega_{r_i})$$

where the integer k represents the number of pressure rakes to be searched. By rotating or stepping the sector around the array of probes, it is possible to compute the maximum valued sector at any time. By plotting the maximum value of the index versus time, a graph similar to Figure 24 could be analyzed for a possible critical value. A time history statistical comparison of deviation from the mean value of the index is another possible test to be applied and is done by Vann [Ref. 4] after adapting this proposed index to existing digital computer programs and comparing it with other known indices.

It is implied that the index is a positive number at all times. There is nothing in the formulation that requires the index to be positive, and if the sector over which the index is computed is small enough then it may in fact be negative. Throughout this paper the term stall has been applied to large inlet flow angles that load the blade row beyond the stall limit of the individual blades. If the inlet flow angle is too small, a phenomenon known as negative stall occurs. Reference 8 discusses the phenomenon of negative stall, but it is important to point out that a negative distortion index would not indicate a negative stall. In the analysis of this index by Vann [Ref. 4],

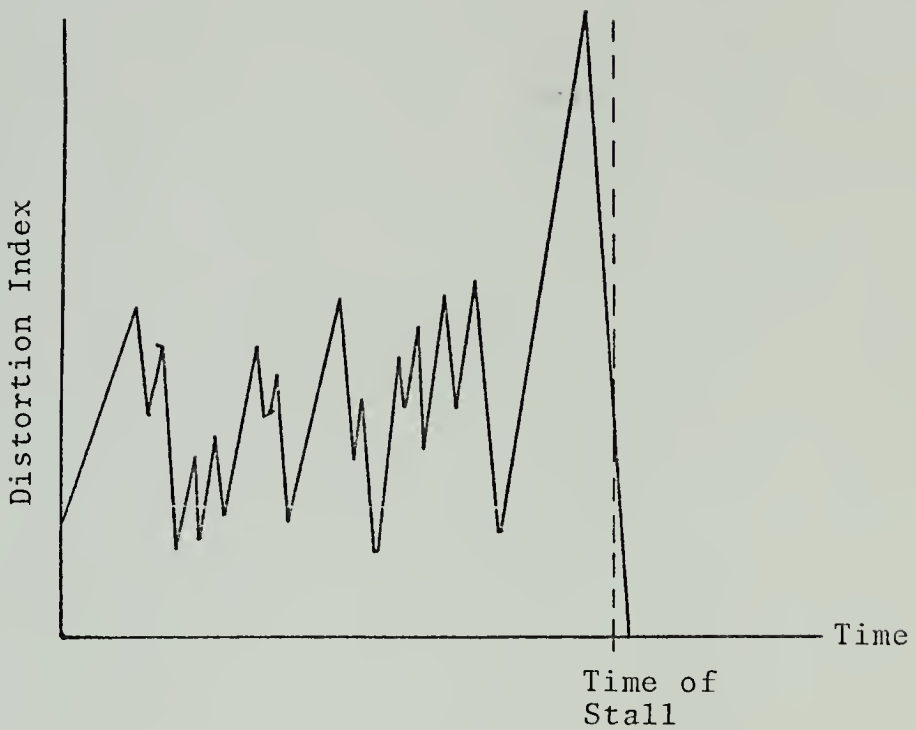

Figure 24. Distortion Index vs. Time.

a sector of 60° was used, and the index values were always positive. Reference 4 addresses the size of sector used to compute this index and other commonly used indices.

VII. CONCLUSIONS

Interpretation of distorted inlet flow interaction with a compressor based on vorticity maps [Refs. 1-3] is satisfactory as long as the assumption of constant static pressure is valid. Experiment has shown that constant static pressure is not the case at the compressor face, and the vorticity model must be expanded to account for this. The failure of the vorticity model to predict the conditions at the face of a compressor (and thus its loss of stall margin) in the case of total temperature distortion is a result of not considering the effects of the compressor on the upstream flow field. The upstream influence of the compressor causes an area change of the undistorted streamtube that results in greater velocity changes than those induced by the vortex itself. The pressure ratio equation, Equation (37), and parallel compressor theory adequately predict trends in compressor stability.

A model based on the bending of the vortex sheet gives results comparable to parallel compressor theory and in the case of total pressure distortion qualitatively duplicates Carta's results.

Carta's stall incidence angle ratio suggests a distortion index that combines radial vorticity and total pressure gradients since both can be related to blade loadings that cause stall. Such an index has been developed and has been

tested [Ref. 4] against other distortion indices using common data for comparison. The new distortion index has proven equal to or better than the distortion indices with which it was compared for accuracy in predicting compressor stall.

APPENDIX A

Ingestion of hot gas from forward firing armament systems has more than temperature effects on the performance of an axial-flow compressor. The characteristic line of corrected engine rotational speed ($N/\sqrt{\theta}$ = constant) appears to be a function of temperature alone since θ is defined as the ratio of actual temperature to some reference temperature, usually a sea level standard day temperature. However, the reference to temperature alone is a convention that has evolved from the fact that compressors in gas turbine engines for aircraft applications use only air as a fluid medium. The corrected engine rotational speed ($N/\sqrt{\theta}$), sometimes identified as referred speed, is a similarity parameter designed to ensure comparability of data taken under varying conditions of testing. In the case of a compressor blade row it is desirable to preserve the blade angle of attack. Consider two "different" compressors as in Figure A-1. If the angle of attack is to remain the same for both compressors, then β must be equal to β'. β is the inlet flow angle but differs from the angle of attack only by a constant related to blade geometry as discussed in Appendix B. For similarity

$$\tan \beta = \frac{\Omega r}{U_z} = \frac{\Omega' r'}{U'_z}$$

and M must equal M'. Therefore

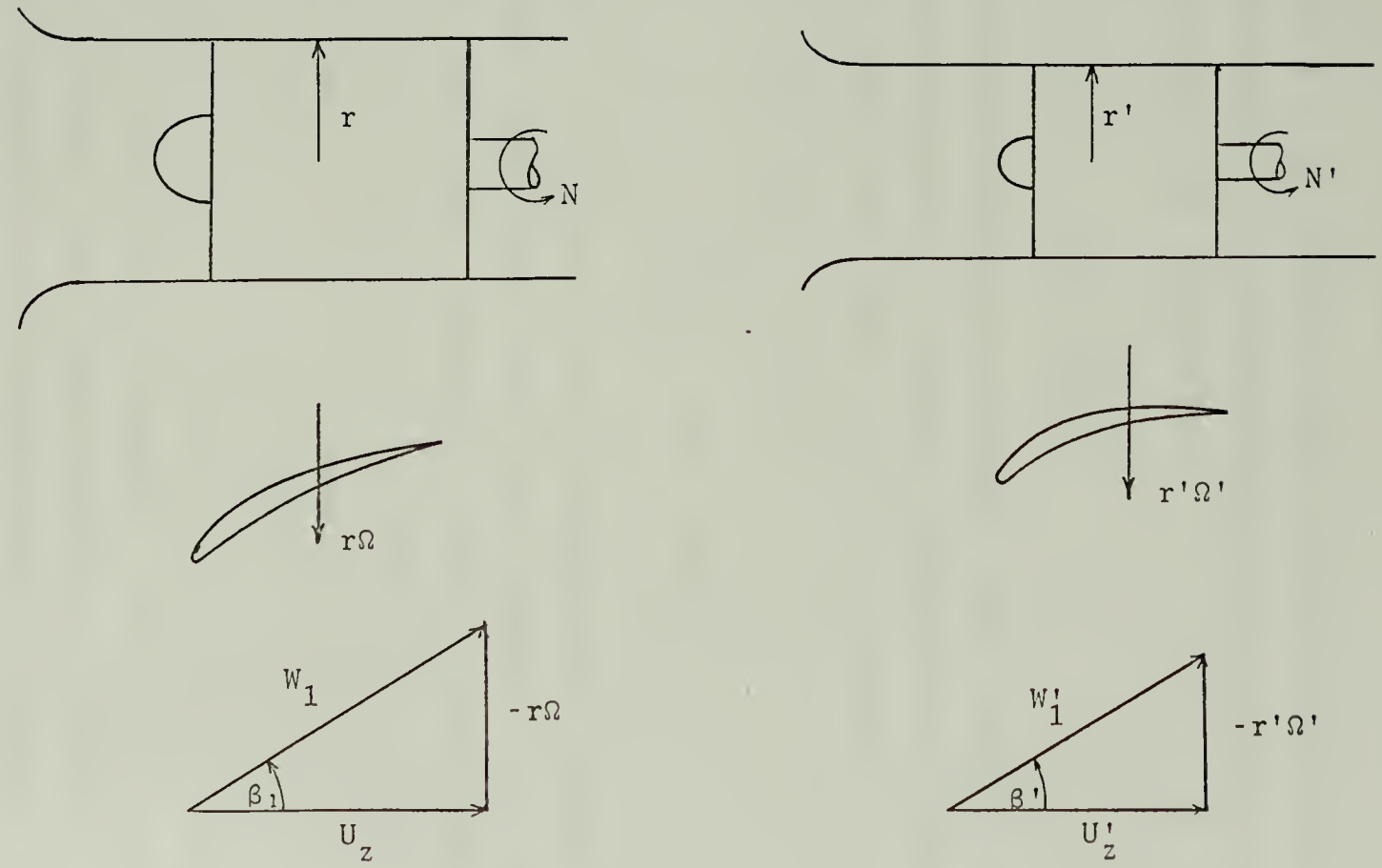

Figure A-1. Similarity for Compressors.

$$\frac{\Omega r}{aM} = \frac{\Omega' r'}{a'M'}$$

where a is the speed of sound. Cancelling the Mach numbers and substituting N (usually RPM) for the angular speed Ω, one obtains the relationship

$$\frac{Nr}{a} = \frac{N'r'}{a'} \quad .$$

Since the compressor performance maps usually relate the characteristics of a specific compressor under differing conditions, the radius r could be eliminated and the similar rotational speeds expressed as

$$\frac{N}{a} = \frac{N'}{a'} \text{ , or } N = N' \frac{a}{a'} \quad .$$

Since $a^2 = \gamma RT$, the ratio of sonic speeds reduces to the ratio of the square root of the temperature if γ and R are the same for both compressors. This is usually the case since γ is a constant for air within the temperature range encountered and $\gamma = \gamma'$ is fundamental to similarity. The gas constant R varies with molecular weight, however; and if the fluid medium is air plus foreign gas (steam or products of combustion for example), then the similarity relationship must retain sonic velocity as a variable. In fact some literature (in particular older literature) uses the corrected rotational speed notation of

$$N_{std} = \frac{N_{actual}\sqrt{L}}{a}$$

where L is a characteristic length, usually the tip radius of the first stage if comparing different sized compressors.

All corrected rotational speeds in this paper are the more usual $N/\sqrt{\theta}$ since foreign gas distortion is not considered. References 2 and 3 analyze the effects of foreign gas distortion or vorticity and how it affects compressor performance.

APPENDIX B

Carta and Adamczyk [Ref. 10] define a stall angle parameter σ as the ratio of instantaneous incidence angle to the stall incidence angle of the compressor blade. They further define the incidence angle α to be the difference between the stagger angle λ and the inlet flow angle β_1. From Figure 14

$$\alpha = \beta_1 - \lambda, \text{ or } \beta_1 = \alpha + \lambda$$

and β_1 differs from α only by a constant λ that is a function of blade geometry. It will not be inconsistent then to plot a distribution of inlet flow angle β_1 vs θ^* instead of σ vs θ^* as in Ref. 10.

In this semi-quantitative analysis a nominal clean inlet (undistorted) value of 45° will be assumed for β_1. The changes in inlet flow angle at the points A, B, B', C, D and E of Figure 17, using the change in U_z and U_θ of Figures 17 and 21, are predicted graphically in Figure B-1. The predicted inlet flow angles are plotted in Figure 21 with the stall parameter σ from Ref. 10.

Although the magnitude of many of the variables in this semi-quantitative analysis are somewhat arbitrary, the directions in which they were applied have been developed carefully in the text of this paper. Deviations from the magnitude used should give the same general shape of inlet

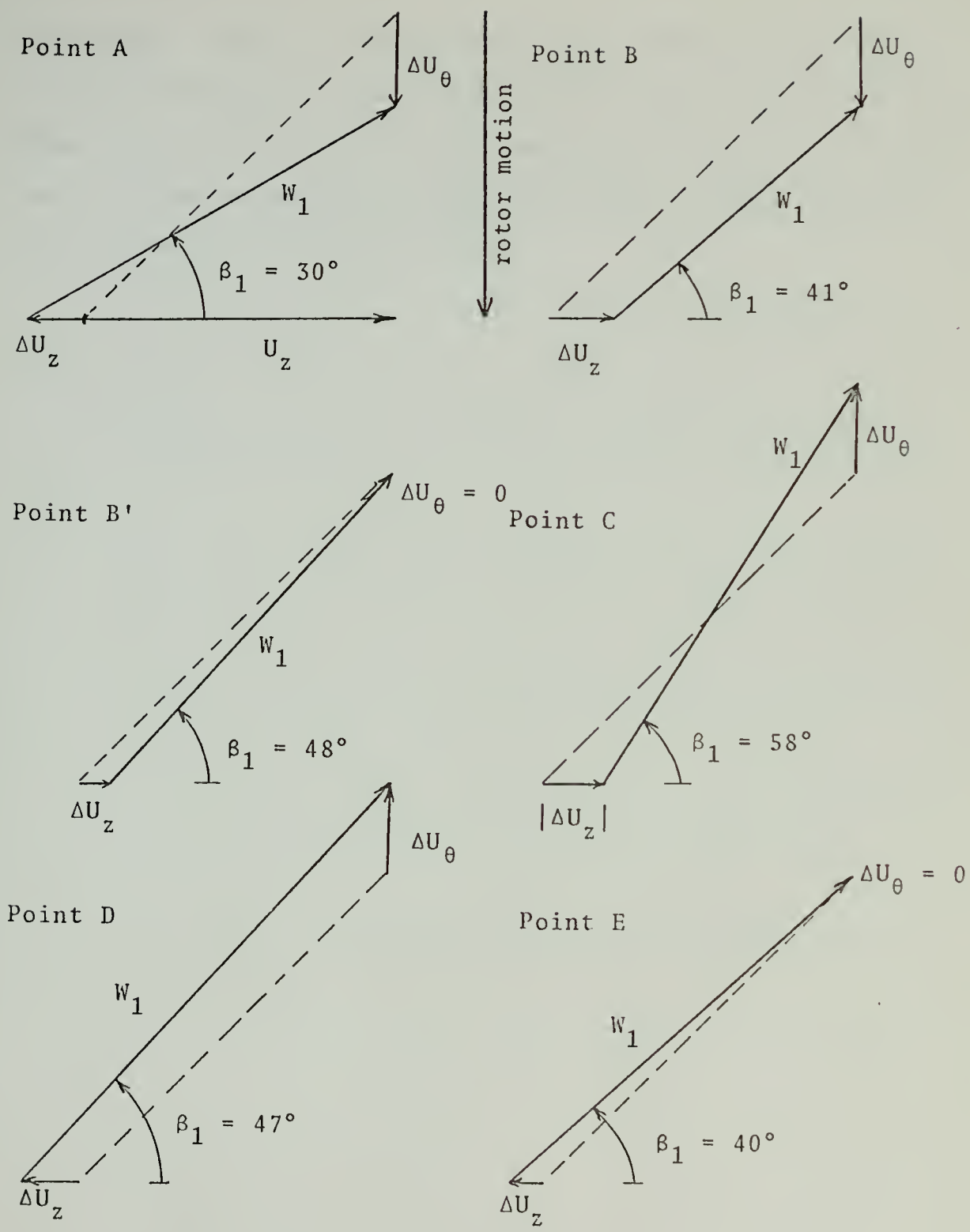

-------W_1 for nominal clean inlet (45°)

Figure B-1. Compressor Effects on Inlet Flow Angle.

flow angle curve as that of Figure 21. The important point is that the general trend of inlet flow angle closely parallels that calculated by Carta and Adamczyk and reinforces the bent vortex model as having accounted for the upstream effect of the compressor on the flow field.

LIST OF REFERENCES

1. Farmer, C. J., Inlet Distortion, Vorticity, and Stall in an Axial Flow Compressor, Master's Thesis, Naval Postgraduate School, Monterey, California, 1972.

2. Iverson, M. M., Conversion of Inlet Temperature Distortions to Vorticity for an Axial-Flow Compressor, Master's Thesis, Naval Postgraduate School, Monterey, California, 1972.

3. Shoemaker, J. E., An Analytical Analysis of the Effects of Instantaneous Vorticity on Compressor Performance, Master's Thesis, Naval Postgraduate School, Monterey, California, 1973.

4. Vann, J. L., Formulation and Comparison of Instantaneous Distortion Indices for Assessing Compressor Stall, Master's Thesis, Naval Postgraduate School, Monterey, California, 1974.

5. AIAA Paper No. 73-1316, The Effect of Inlet Temperature and Pressure Distortion on Turbojet Performance, by W. M. Braithwaite, E. J. Graber, Jr., and C. M. Mehalic, November 1973.

6. AIAA Paper No. 72-1116, A New Approach to Distortion Induced Compressor Stall--Vorticity Maps, by LT Clinton Farmer, LCDR Michael Iverson and Allen Fuhs, 1972.

7. Shapiro, A. H., The Dynamics and Thermodynamics of Compressible Fluid Flow, Volume 1, The Ronald Press Company, 1953.

8. Hill, P. G., and Peterson, C. R., Mechanics and Thermodynamics of Propulsion, Addison-Wesley, 1965.

9. Vavra, M. H., Aero-Thermodynamics and Flow in Turbomachines, Wiley, 1960.

10. Carta, F. O. and Adamczyk, J. J., "Unsteady Fluid Dynamic Response of an Axial-Flow Compressor Stage with Distorted Inflow," Project SQUID Technical Report UARL -2-PU, July 1973.

INITIAL DISTRIBUTION LIST

		No. Copies
1.	Defense Documentation Center Cameron Station Alexandria, Virginia 22314	2
2.	Library, Code 0212 Naval Postgraduate School Monterey, California 93940	2
3.	Chairman, Department of Aeronautics Naval Postgraduate School Monterey, California 93940	1
4.	Professor Allen E. Fuhs Department of Aeronautics Naval Postgraduate School Monterey, California 93940	5
5.	LCDR Charles Patrick Downs, USN 6200 N.W. 8th Street Oklahoma City, Oklahoma 73127	3
6.	ENS James E. Shoemaker 113 Norton Street Bennington, Vermont 05201	1
7.	Professor M. F. Platzer Department of Aeronautics Naval Postgraduate School Monterey, California 93940	1
8.	Mr. Joe Boytos Naval Air Propulsion Test Center Trenton, New Jersey 08628	1
9.	Dr. Herbert Mueller Code 310A Naval Air Systems Command Washington, D. C. 20360	1
10.	Dr. Frank Tanczos Code 03 Naval Air Systems Command Washington, D. C. 20360	1

11. Mr. Karl Guttman — 1
Code 330
Naval Air Systems Command
Washington, D. C. 20360

12. Dr. H. O. Johnson — 1
Code 330
Naval Air Systems Command
Washington, D. C. 20360

13. Mr. Robert Brown — 1
Code 536
Naval Air Systems Command
Washington, D. C. 20360

14. Dr. Ralph Roberts — 1
Office of Naval Research
800 North Quincy Street
Arlington, Virginia 22217

15. Mr. Eric Lister — 1
R. & T. Division
Naval Air Propulsion Test Center
Trenton, New Jersey 08628

16. Mr. Albert Martino — 1
R. & T. Division
Naval Air Propulsion Test Center
Trenton, New Jersey 08628

17. Mr. James Patton, Jr. — 1
Office of Naval Research
Arlington, Virginia 22218

18. M. l'Ingenieur en Chef Marc Pianko — 1
Service Technique Aeronautique
4 Avenue de la Porte d'Issy
75 Paris 15eme FRANCE

19. Mr. J. Surugue — 1
Directeur, Energie et Propulsion
ONERA
29 Avenue de la Division Leclerc
92 Chatillon-sous-Bagneux, FRANCE

20. Mr. John Dunham — 1
National Gas Turbine Establishment
Pyestock
Farnborough Hants GREAT BRITAIN

21. Professor Kuhl — 1
D. V. L.
505 Porz Wahn
Linder Hohe
Allemagne GERMANY

22. Mr. Clifford Simpson — 1
AFAPL/TB
Wright-Patterson A.F.B., Ohio 45433

23. Professor Gordon Oates — 1
University of Washington
Seattle, Washington 98105

24. Professor Robert Goulard — 1
Director, Project SQUID
Purdue University
Lafayette, Indiana

25. Mr. J. F. Chevalier — 1
SNECMA
Centre d'Essais de Villaroche
77 Moissy-Cramayel FRANCE

26. Mr. M. Van Staveren — 1
Institute for Applied Research TNO
Post bus 406
Delft NETHERLANDS

27. Mr. Hillard Barrett — 1
Detroit Diesel Allison
General Motors Corp.
Indianapolis, Indiana 46206

28. Mr. Elmer G. Johnson — 1
Director, Fluid Dynamics Facilities Research Laboratory
USAF Aerospace Research Laboratories
WPAFB, Ohio 45433

29. Dr. A. A. Mikolajczak — 1
Pratt and Whitney Aircraft
East Hartford, Connecticut 06198

30. Dr. Peter Tramm — 1
Detroit Diesel Allison
General Motors Corp.
Indianapolis, Indiana 46206

31. Professor Duncan Rannie — 1
California Institute of Technology
Pasadena, California 91109

32. Professor Jack Kerrebrock — 1
Aeronautics and Astronautics
Massachusetts Institute of Technology
Cambridge, Massachusetts 02138

33. Professor George Serovy — 1
Iowa State University
Ames, Iowa 50010

34. Dr. Gary R. Ludwig, Aerodynamics Research — 1
CALSPAN Corp.
Buffalo, New York 14221

35. Mr. James E. Calogeras — 1
NASA Lewis Research Center
Cleveland, Ohio 44135

36. Dr. Gunnar Broman — 1
Vice President, Engineering
VOLVE Flygmotor
Trollhattan, SWEDEN

37. Mr. Robert Zalis — 1
MZ 240 GF
1000 Western Avenue
Lynn, Massachusetts 01910

38. Mr. Paul H. Kutschenreuter, Jr. — 1
Mail Drop E 198
General Electric Company
Cincinnati, Ohio 45215

39. Professor Jacques Valensi — 1
Director Institut de Mecanique des Fluides
1'Universite d'Aix-Marseille
Marseille, FRANCE

40. Professor Jacques Chauvin — 1
Von Karman Institute for Fluid Mechanics
72 Chaussee de Waterloo
1640 Rhode-St-Genese BELGIUM

41. Mr. Marvin F. Schmidt — 1
Turbine Engine Division
AFAPL
WBAFB, Ohio 45433

42. Mr. J. W. McBride — 1
General Electric Company
Evandale, Ohio 45215

43. Dr. Leroy H. Smith, Jr. — 1
General Electric Company
Evandale, Ohio 45215

44. Professor B. Lakshminarayana — 1
MIT Gas Turbine Laboratory
Massachusetts Institute of Technology
Cambridge, Massachusetts 02138

45. Professor Jean Louis 1
MIT Gas Turbine Laboratory
Massachusetts Institute of Technology
Cambridge, Massachusetts 02138

46. Dr. F. O. Carta 1
United Aircraft Research Labs.
United Aircraft Corporation
400 Main Street
East Hartford, Connecticut 06108

47. Mr. Norman Cotter 1
Pratt and Whitney Florida Research Center
West Palm Beach, Florida 33402

48. Dr. George L. Mellor 1
Princeton University
Forrestal Campus
Princeton, New Jersey 08540

49. Mr. Stan Ellis 1
Pratt and Whitney Florida Research Center
West Palm Beach, Florida 33402

50. Mr. David Bowditch 1
NASA Lewis Research Center
Cleveland, Ohio 44135

51. Professor Frank Marble 1
California Institute of Technology
Pasadena, California 91109

52. Professor Bruce A. Reese 1
School of Mechanical Engineering
Purdue University
Lafayette, Indiana 47907

53. Professor T. C. Adamson, Jr. 1
Dept. of Aerospace Engineering
University of Michigan
Ann Arbor, Michigan 48103

54. Professor W. R. Sears 1
University of Arizona
Tucson, Arizona

55. Professor J. E. McCune 1
M. I. T. - 37 - 391
Cambridge, Massachusetts 02139

56. Dr. Jack Nielsen 1
Nielsen Engineering and Research, Inc.
850 Maude Avenue
Mountain View, California 94040

57. W. F. O'Brien 1
Mechanical Engineering Dept.
Virginia Polytechnic Institute and State University
Blacksburg, Virginia 24061

58. Dr. W. Heiser 1
AFAPL
WPAFB, Ohio 45433

59. CAPT Barry Brownstein 1
Air Force Aero-Propulsion Laboratory
Wright-Patterson A.F.B., Ohio 45433

60. Mr. Paul Burstadt 1
NASA Lewis Research Center
Cleveland, Ohio 44135

61. LT John Vann 1
1840 Lynnhaven Road
Ft. Worth, Texas

62. Mr. Ivan Bush 1
Air Force Aero-Propulsion Laboratory
Wright-Patterson A.F.B., Ohio 45433

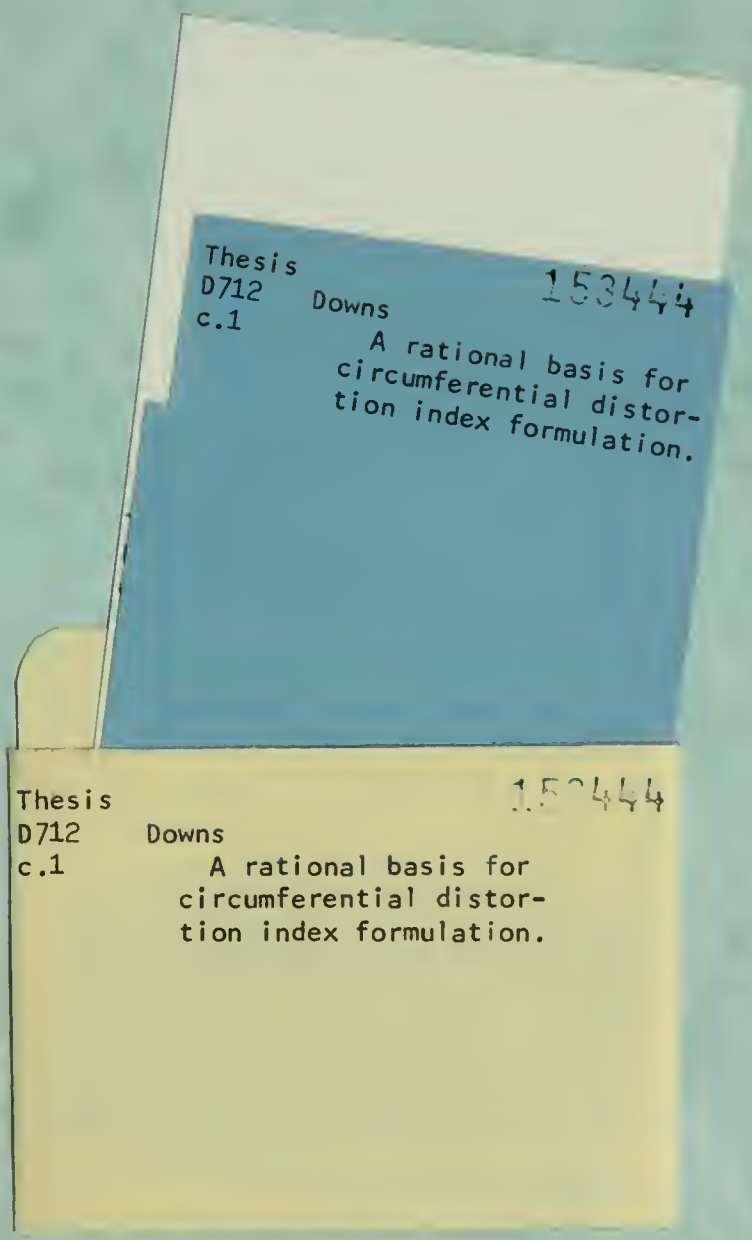

Thesis
D712 Downs
c.1 A rational basis for circumferential distortion index formulation.
153444